The Astrophysical Journal, 973:99 (22pp), 2024 October 1 https://doi.org/10.3847/1538-4357/ad63a0

Ne VIII in the Warm-hot Circumgalactic Medium of FIRE Simulations and in Observations

Nastasha A. Wijers[1], Claude-André Faucher-Giguère[1], Jonathan Stern[2], Lindsey Byrne[1], and Imran Sultan[1]
[1] CIERA and Department of Physics and Astronomy, Northwestern University, 1800 Sherman Ave, Evanston, IL 60201, USA; nastasha.wijers@northwestern.edu
[2] School of Physics & Astronomy, Tel Aviv University, Tel Aviv 69978, Israel
Received 2024 January 16; revised 2024 July 11; accepted 2024 July 14; published 2024 September 23

Abstract

The properties of warm-hot gas around $\sim L_*$ galaxies can be studied with absorption lines from highly ionized metals. We predict Ne VIII column densities from cosmological zoom-in simulations of halos with masses in $\sim 10^{12}$ and $\sim 10^{13}\,M_\odot$ from the Feedback in Realistic Environments (FIRE) project. Ne VIII traces the volume-filling, virial-temperature gas in $\sim 10^{12}\,M_\odot$ halos. In $\sim 10^{13}\,M_\odot$ halos the Ne VIII gas is clumpier, and biased toward the cooler part of the warm-hot phase. We compare the simulations to observations from the COS Absorption Survey of Baryon Harbors (or CASBaH) and COS Ultraviolet Baryon Survey (or CUBS). We show that when inferring halo masses from stellar masses to compare simulated and observed halos, it is important to account for the scatter in the stellar-mass–halo-mass relation, especially at $M_\star \gtrsim 10^{10.5}\,M_\odot$. Median Ne VIII columns in the fiducial FIRE-2 model are about as high as observed upper limits allow, while the simulations analyzed do not reproduce the highest observed columns. This suggests that the median Ne VIII profiles predicted by the simulations are consistent with observations, but that the simulations may underpredict the scatter. We find similar agreement with analytical models that assume a product of the halo gas fraction and metallicity (relative to solar) ~ 0.1, indicating that observations are consistent with plausible circumgalactic medium temperatures, metallicities, and gas masses. Variants of the FIRE simulations with a modified supernova feedback model and/or active galactic nuclei feedback included (as well as some other cosmological simulations from the literature) more systematically underpredict Ne VIII columns. The circumgalactic Ne VIII observations therefore provide valuable constraints on simulations that otherwise predict realistic galaxy properties.

Unified Astronomy Thesaurus concepts: Circumgalactic medium (1879); Galaxy groups (597); Galaxy formation (595); Quasar absorption line spectroscopy (1317); Hydrodynamical simulations (767)

1. Introduction

The circumgalactic medium (CGM), a halo of gas surrounding galaxies, plays an important role in galaxy formation and evolution (e.g., the review by Tumlinson et al. 2017). If this gas accretes onto the central galaxy, it can form stars. Conversely, cutting off accretion onto a central galaxy can quench it (see, e.g., the review by Faucher-Giguère & Oh 2023). This can occur due to the feedback from the central galaxy (stars and active galactic nuclei, AGN), which can heat interstellar medium (ISM) gas and eject it into the CGM. It can also heat the CGM, and possibly generate outflows that escape the halo altogether (e.g., Muratov et al. 2015, 2017; Hafen et al. 2020; Pandya et al. 2020; Mitchell & Schaye 2022).

This means that understanding the CGM can help us understand the processes that regulate galaxy formation. However, we currently do not know how much mass there is in the CGM around L_* (halo mass $\sim 10^{12}\,M_\odot$) galaxies (Werk et al. 2014). Halos around this mass, roughly $\sim 10^{12}$–$10^{13}\,M_\odot$, are interesting, as these halos are where central galaxy quenching mostly occurs (e.g., Behroozi et al. 2019). This is the mass range we will investigate in this paper.

We have many observations of cool CGM gas ($\sim 10^4$ – 10^5 K) from UV absorption-line observations (e.g., Tumlinson et al. 2017), from which we can infer its temperature, density, metallicity, and mass. There are also many detections of O VI absorption. This can come from warmer gas at $\sim 10^{5.5}$ K, but it can also trace cool, photoionized gas.

The warm-hot, virialized CGM gas phase is where CGM mass estimates are most uncertain (Werk et al. 2014). Its absorption and emission lines are largely in the X-ray band (e.g., Hellsten et al. 1998; Perna & Loeb 1998; Chen et al. 2003; Cen & Fang 2006; Branchini et al. 2009), where absorption-line detections are rare and do not often reach high significance (e.g., Nicastro 2016). There is a larger sample of X-ray observations of the Milky Way halo (e.g., Bregman & Lloyd-Davies 2007; Gupta et al. 2014; Miller & Bregman 2015; Gupta et al. 2017; Das et al. 2019), but as this is a single system, it can be difficult to draw conclusions about the CGM in general from these.

Planned and proposed future instruments such as the Athena X-IFU (Nandra et al. 2013; Barret et al. 2018), Arcus (Smith et al. 2016), Line Emission Mapper (Kraft et al. 2022), HUBS (Cui et al. 2020), and Lynx (The Lynx Team 2018) can give us the X-ray absorption- and emission-line data we need (e.g., Wijers et al. 2020; Wijers & Schaye 2022; Nelson et al. 2023). However, current X-ray instruments do not have the sensitivity and spectral resolution required to observe the CGM of a large set of $\sim L_*$ halos. Fast radio burst (FRB) dispersion measures (e.g., McQuinn 2014) and measurements of the Sunyaev–Zel'dovich (SZ) effect (e.g., the review by Mroczkowski et al. 2019) could also provide future constraints on the CGM ionized gas content, but robust measurements of the CGM content of Milky Way–like halos will require larger samples of localized FRBs (e.g., Ravi 2019) or instrumental improvements

for SZ measurements such as a higher spatial resolution (Mroczkowski et al. 2019).

Therefore, in this paper, we focus on an extreme UV absorption line: the Ne VIII doublet at 770, 780 Å. Burchett et al. (2019) and Qu et al. (2024) completed the COS Absorption Survey of Baryon Harbors (CASBaH) and COS Ultraviolet Baryon Survey (CUBS), respectively, for Ne VIII absorption in quasar spectra, and obtained galaxy observations along the quasar sightlines. This allows them to associate the absorbers with the halos of specific galaxies. Ne VIII ion fractions peak at $\approx 10^{5.6}$–$10^{6.2}$ K in collisional ionization equilibrium (CIE). We define this peak as the range of temperatures where the ion fraction is at least 0.1× the maximum CIE ion fraction. This peak temperature range makes Ne VIII a good candidate to trace the warm-hot, volume-filling gas in $\sim 10^{12}\,M_\odot$ halos (e.g., Verner et al. 1994).

We use a multipronged approach to study the physical nature of Ne VIII in the CGM. We start with a theoretical analysis of the properties of Ne VIII in cosmological zoom-in simulations from the Feedback In Realistic Environments (FIRE) project, compare different simulation variants with observations, and further explore more general insights that can be extracted using idealized analytic models.[3] In Section 2, we describe the FIRE-2 and FIRE-3 simulations we analyze, and how we predict column densities from them. Next, in Section 3, we explore the properties of Ne VIII in the halos we study. In Section 4, we then describe how the FIRE predictions compare to the observations. Next, we explore a simple analytical model for Ne VIII column densities in Section 5. In Section 6, we compare our results to others in the literature. Finally, we summarize our results in Section 7.

We use a flat Lambda cold dark matter (ΛCDM) cosmology, with a redshift 0 Hubble parameter in units of $100\,\mathrm{km\,s^{-1}Mpc^{-1}}$ of $h \approx 0.7$, and cosmic mean densities of dark energy and total matter, normalized to the critical density, of $\Omega_\Lambda \approx 0.7$ and $\Omega_m \approx 0.3$, respectively. We analyze each simulation using the exact parameter set it was run with. Distances measured in kiloparsec use physical/proper kiloparsec, unless specified otherwise.

2. Methods

We analyze simulations run with four different physics models: one fiducial FIRE-2 model and three FIRE-3 models. The FIRE-3 models have either no AGN feedback, AGN feedback without cosmic rays (CRs), or AGN feedback with CRs. Below, we describe these simulations in more detail, and briefly explain how we predict column densities from them.

2.1. The FIRE-2 Simulations

The FIRE-2 simulations are described in detail in Hopkins et al. (2018a). The simulations use the meshless finite mass (MFM) magnetohydrodynamics solver (Hopkins 2015), in the GIZMO code (Hopkins 2015).[4]

In the FIRE-2 simulations, 11 elements are explicitly tracked, including neon. The radiative cooling and heating calculations (Hopkins et al. 2018a) include processes relevant to the cool and cold ISM, such as cooling from molecules and fine structure lines. The cooling and heating processes are applicable to temperatures of 10–10^{10} K. For temperatures $>10^4$ K, metal-line cooling follows Wiersma et al. (2009). The effects of ionizing photons from both a Faucher-Giguère et al. (2009) background and stars in the simulations are included. For radiation from stars, a radiative transfer method with a self-shielding approximation is used (LEBRON; Hopkins et al. 2012, 2018a).

Star formation can occur in gas if it is (i) self-gravitating (the potential energy is larger than the thermal and kinetic energy combined), (ii) self-shielding (it contains molecular gas), (iii) Jeans unstable (the thermal Jeans mass is smaller than the resolution element mass), and (iv) has a minimum density $n_H > 10^3\,\mathrm{cm^{-2}}$. The star formation rate (SFR) is then simply the molecular gas density over the freefall time of the resolution element. Star particles represent a single-age stellar population, and have the mass and element abundances of the gas particles they formed from. The feedback from each single-age stellar population is taken from STARBURST99 (Leitherer et al. 1999), assuming a Kroupa (2001) stellar initial mass function and a stellar mass range of 0.1–100 $M_\odot$. This includes supernova (SN) rates and abundances, mass, and energy in SNe and in stellar winds. The injected SN momentum and energy depend on the Sedov–Taylor solution for the explosion, given the density and mass of the surrounding gas (Martizzi et al. 2015; Hopkins et al. 2018b).

The FIRE-2 simulations we analyze include a prescription for subgrid metal diffusion (Colbrook et al. 2017; Hopkins et al. 2018a). The FIRE-2 model contains neither black holes (BHs), nor CRs, so we will label it "FIRE-2 NoBH". These simulations have redshift 0 main halo masses of $\sim 10^{12}\,M_\odot$, and are listed in Table 1.

2.2. The FIRE-3 Simulations

The FIRE-3 simulations are a set of simulations run with similar stellar physics models but using the FIRE-3 code (Hopkins et al. 2023). Much of the modeling is the same as in the FIRE-2 simulations, with some updates. The FIRE-3 simulations include magnetic fields (Hopkins & Raives 2016; Hopkins 2016), unlike our FIRE-2 sample. In the FIRE-3 NoBH simulations, the magnetic pressure in the CGM is generally <0.1 times the thermal pressure (with fractions <0.01 typical; I. Sultan et al. 2024, in preparation), meaning its dynamical effect is likely small. This is consistent with the small differences previously reported between the FIRE-2 runs with and without magnetic fields (Hopkins et al. 2020), and the small effects of magnetic fields on the CGM Su et al. (2019) found for a FIRE-2 m12 halo. Note that this is different from what van de Voort et al. (2021) found for zoom-in simulations run with the IllustrisTNG and Auriga feedback models. In those simulations, magnetic fields are dynamically more important in the CGM.

The UV/X-ray background was updated to that of Faucher-Giguère (2020). When calculating ion fractions, we will use the Ploeckinger & Schaye (2020a) tables, produced by Ploeckinger & Schaye (2020b), who also assumed a Faucher-Giguère (2020) UV/X-ray background.[5] Stellar evolution and feedback modeling were also updated, and the star formation criteria from FIRE-2 were adjusted for FIRE-3: the gas must be (i) self-gravitating, (ii) Jeans unstable, and (iii) converging or not

[3] See the FIRE project website: https://fire.northwestern.edu/.

[4] The public GIZMO version is available at http://www.tapir.caltech.edu/~phopkins/Site/GIZMO.html.

[5] We specifically use the UVB_dust1_CR1_G1_shield1.hdf5 table.

Table 1
The FIRE-2 and FIRE-3 Simulations Analyzed in This Work

ICs	Model	Resolution ($M_\odot$)	$z = 1.0$			$z = 0.5$		
			$M_{\rm vir}$ ($M_\odot$)	$M_\star$ ($M_\odot$)	$R_{\rm vir}$ (pkpc)	$M_{\rm vir}$ ($M_\odot$)	$M_\star$ ($M_\odot$)	$R_{\rm vir}$ (pkpc)
m12r	FIRE-2 NoBH	7e3	2.9e11	2.6e9	103	3.5e11	4.6e9	139
m12z	FIRE-2 NoBH	4e3	3.2e11	9.1e8	107	5.2e11	2.7e9	160
m12w	FIRE-2 NoBH	7e3	4.1e11	3.6e9	115	8.7e11	1.1e10	188
m12c	FIRE-2 NoBH	7e3	6.0e11	5.1e9	132	6.9e11	1.9e10	176
m12b	FIRE-2 NoBH	7e3	6.8e11	2.5e10	138	1.2e12	4.7e10	212
m12f	FIRE-2 NoBH	7e3	7.2e11	9.6e9	141	1.1e12	2.4e10	203
m12m	FIRE-2 NoBH	7e3	8.1e11	5.3e9	147	1.1e12	2.7e10	206
m12i	FIRE-2 NoBH	7e3	8.4e11	1.0e10	149	8.3e11	2.7e10	187
m12r	FIRE-3 NoBH	7e3	2.8e11	1.6e9	101	3.5e11	2.7e9	139
m12z	FIRE-3 NoBH	4e3	2.8e11	6.8e8	103	4.6e11	8.0e8	153
m12w	FIRE-3 NoBH	7e3	3.8e11	2.4e9	112	7.6e11	3.4e9	180
m12f	FIRE-3 NoBH	7e3	6.8e11	4.0e9	138	9.9e11	6.7e9	199
m12q	FIRE-3 NoBH	7e3	8.3e11	5.1e9	148	1.2e12	9.2e9	212
m13h206	FIRE-3 NoBH	3e5	4.3e12	1.2e11	253	6.1e12	2.2e11	363
m13h113	FIRE-3 NoBH	3e5	5.6e12	1.0e11	276	8.2e12	2.6e11	400
m13h236	FIRE-3 NoBH	3e5	6.0e12	1.1e11	282	8.3e12	2.2e11	401
m13h007	FIRE-3 NoBH	3e5	8.4e12	9.7e10	316	1.4e13	1.6e11	477
m13h029	FIRE-3 NoBH	3e5	9.1e12	1.3e11	324	1.2e13	3.0e11	453
m13h002	FIRE-3 NoBH	3e5	1.5e13	1.4e11	379	2.2e13	2.3e11	552
m13h223	FIRE-3 NoBH	3e5	1.6e13	1.1e11	395	2.1e13	2.5e11	546
m12r	FIRE-3 BH	7e3	2.8e11	2.0e9	102	3.5e11	3.1e9	139
m12w	FIRE-3 BH	7e3	3.8e11	3.5e9	112	8.2e11	6.3e9	185
m12b	FIRE-3 BH	7e3	6.0e11	4.5e9	132	1.1e12	8.0e9	205
m12m	FIRE-3 BH	7e3	6.3e11	3.5e9	135	9.9e11	6.9e9	199
m12f	FIRE-3 BH	7e3	6.6e11	5.6e9	137	1.0e12	8.5e9	201
m12i	FIRE-3 BH	7e3	7.8e11	4.9e9	144	7.3e11	8.1e9	179
m12q	FIRE-3 BH	7e3	8.3e11	4.9e9	148	1.1e12	7.3e9	209
m13h206	FIRE-3 BH	3e4	4.3e12	4.8e10	252	6.1e12	1.2e11	362
m13h113	FIRE-3 BH	3e4	5.3e12	3.4e10	270	8.1e12	8.9e10	398
m12f	FIRE-3 BHCR	6e4	6.3e11	3.5e9	135	1.0e12	3.9e9	200
m12m	FIRE-3 BHCR	6e4	6.5e11	5.1e9	136	8.4e11	8.6e9	188
m12i	FIRE-3 BHCR	6e4	7.5e11	4.1e9	143	6.9e11	5.1e9	176
m12q	FIRE-3 BHCR	6e4	8.1e11	3.1e9	147	1.2e12	3.8e9	209
m13h206	FIRE-3 BHCR	3e5	3.9e12	3.8e10	244	5.7e12	4.3e10	354
m13h113	FIRE-3 BHCR	3e5	4.9e12	2.9e10	263	7.4e12	3.6e10	386
m13h236	FIRE-3 BHCR	3e5	5.1e12	2.4e10	268	7.2e12	2.9e10	383
m13h007	FIRE-3 BHCR	3e5	7.5e12	4.1e10	304	1.2e13	4.7e10	457
m13h029	FIRE-3 BHCR	3e5	8.5e12	3.7e10	318	1.0e13	5.2e10	433
m13h002	FIRE-3 BHCR	3e5	1.2e13	2.7e10	353	1.7e13	3.7e10	513
m13h037	FIRE-3 BHCR	3e5	1.4e13	4.8e10	374	1.9e13	5.9e10	531
m13h009	FIRE-3 BHCR	3e5	1.9e13	3.2e10	418	2.5e13	3.6e10	584

Note. We show initial conditions (ICs), physics model, resolution (for gas mass resolution elements), and the halo mass, stellar mass, and virial radius for redshifts 1.0 and 0.5.

diverging too rapidly. (A strict minimum density is not required). As for the FIRE-2 simulations, subgrid metal diffusion is included in the simulations we analyze.

The FIRE-3 simulations also include updated stellar yields for SNe (core-collapse and Type Ia SNe) and for stellar winds (Hopkins et al. 2023). The Type Ia yields were updated from the Iwamoto et al. (1999) values to the average of the Leung & Nomoto (2018) W7 and WDD2 models, and the core-collapse yields from Nomoto et al. (2006) to a modified Sukhbold et al. (2016) model. The SN yield updates result in lower neon yields in FIRE-3 than in FIRE-2: the ratio of total neon mass to total stellar mass is larger by a factor of ≈2 in the FIRE-2 simulations we analyze than in our FIRE-3 simulations. The FIRE-2/3 model for stellar winds does not produce neon.

We consider a set of three FIRE-3 physics models. The first includes no AGN feedback (NoBH), the second includes AGN feedback without CRs (BH), and the third includes AGN feedback with CRs (BH+CR). Note that the BH+CR model contains CRs from AGN and SNe, while the other models do not contain CRs from any source. For the FIRE-3 simulations, we consider halos with redshift 0 halo masses of $\sim 10^{12}\,M_\odot$ (m12 halos). Unlike for the FIRE-2 model, we also include more massive m13 halos, with redshift 0 halo masses $\sim 10^{13}\,M_\odot$.

In the BH and BH+CR models, BHs are stochastically seeded from star-forming gas, especially at high surface

densities and low metallicities (Hopkins et al. 2018a; Wellons et al. 2023). They merge if they are close together and gravitationally bound. The BH accretion model is described by Wellons et al. (2023) and Hopkins et al. (2023).

AGN feedback follows Wellons et al. (2023), with the parameters given by Byrne et al. (2023). Radiative feedback is injected at a rate of 0.1 times the accretion rate. Winds are injected (Torrey et al. 2020; Su et al. 2021) at a fixed velocity of $3000\,\mathrm{km\,s^{-1}}$, parallel to the BH angular momentum (Hopkins et al. 2016). The wind mass injection rate is equal to the BH accretion rate. In the BH+CR model, jets are modeled by adding CRs to the created wind resolution elements, with an energy efficiency of 10^{-3} relative to $\dot{M}_{\rm BH}c^2$, where $\dot{M}_{\rm BH}$ is the accretion rate.

In the BH+CR simulations, the CR model evolves the CR spectrum for protons and electrons. The CR scattering rate depends on local plasma properties (Chan et al. 2019; Hopkins et al. 2022a). Specifically, the modified external driving model in Section 5.3.2 of Hopkins et al. (2022b) is used. This model was calibrated to reproduce the Voyager and AMS-02 observations from MeV to TeV energies in Milky Way–like simulations. CRs are injected by SN explosions and stellar winds, making up 10% of the initial kinetic energy in both, and by AGN as described above.

We must stress an important point about the FIRE-3 simulations analyzed in this paper. The FIRE-3 runs we analyze implement a "velocity-aware" numerical method to deposit energy and momentum to gas resolution elements. This scheme improves conservation properties, as described in Hopkins et al. (2023), but introduces significant differences in the net terminal momentum injected following SNe relative to FIRE-2, especially in the regime of locally converging gas flows. In this limit, the momentum injected can be substantially larger than standard models for the terminal momentum in a static medium (e.g., Martizzi et al. 2015; Hopkins et al. 2018b). For the relatively massive halos we study in this paper, this results in galaxy stellar masses in FIRE-3 simulations that are lower than in FIRE-2 (see Hopkins et al. 2023). This change in the momentum deposited by SNe in massive galaxies depends on a nonunique choice for how to implement the subgrid SN physics. This subtlety was not described in the original FIRE-3 methods paper, but is explained in detail in Hopkins (2024).

We note that the FIRE-3 SNe feedback model implemented in the present simulations is not a priori "incorrect" or "unphysical." Rather, it reflects a different theoretical assumption for the unresolved, subgrid dynamics relative to FIRE-2. A priori, both the FIRE-2 model and this FIRE-3 feedback model are reasonable. However, as we will show, our comparison with Ne VIII CGM observations empirically favors the FIRE-2 model. Hopkins (2024) also discusses some theoretical issues with the particular implementation used in the present FIRE-3 runs that could make it less realistic. In future FIRE-3 simulations, we will likely use a modified implementation that produces injected SN momentum, stellar masses, and (presumably) CGM properties in closer agreement with FIRE-2 for the same basic physics (e.g., NoBH). For simplicity, we will simply refer to the present runs as FIRE-3, but caution that the results will not necessarily apply to future FIRE-3 runs with a modified SN model.

2.3. The Simulation Sample

We analyze a set of cosmological zoom simulations of halos with masses $\sim10^{12}\,M_\odot$ (m12) and $\sim10^{13}\,M_\odot$ (m13).

The set of FIRE-2 simulations we analyze comes from the public release of FIRE-2 data by Wetzel et al. (2023). We specifically consider the halos with redshift 0 masses of $\sim10^{12}\,M_\odot$ in the "core" suite.[6] These halos were selected from a cosmological volume based on their mass, and being relatively isolated from halos of similar or higher masses.

Most of the FIRE-3 halos we analyzed were presented in Byrne et al. (2023). The FIRE-3 NoBH m12i simulation was also presented by Hopkins et al. (2023). For a subset of the halos we analyze here, FIRE-3 simulations have been analyzed for central galaxy properties by Byrne et al. (2023) and for other CGM properties by Sultan et al. (2024, in preparation).

We list the halo mass, virial radius, and stellar mass of the central galaxy of each simulation in Table 1. (See Section 2.4 for definitions.) We show these values at redshifts 0.5 and 1.0 since we analyze simulations between these redshifts. This range was selected to roughly match the redshift range searched by Burchett et al. (2019) as part of the CASBaH survey; the Qu et al. (2024) data from the CUBS survey cover a smaller redshift range. We similarly analyzed m12 and m13 halos since the Burchett et al. (2019) and Qu et al. (2024) galaxies likely reside in halos of roughly these masses (see Section 4.1).

For each physics model and halo mass category, we analyzed the halos from simulations that had reached redshift 0.5. This ensured each simulation covered our target redshift range of 0.5–1.0. Within this range, we specifically analyze simulation outputs at redshifts 0.5, 0.6, 0.7, 0.8, 0.9, and 1.0.

Of our halos, only m12f was run for all m12 physics models, and only m13h113 and m13h206 reached redshift 0.5 for all three m13 physics models. In comparisons between physics models, we will therefore often focus on these halos.

2.4. Finding and Centering Our Halos

The halos we analyze are the main halos in each zoom-in volume. We find the halo centers using a shrinking spheres method (Power et al. 2003), starting at the center of mass of the zoom-in region. We use all zoom region resolution elements (high-resolution dark matter, gas, stars, and BHs if included) to determine the halo center. We then find the halo virial radius and mass using the Bryan & Norman (1998) mean enclosed halo density.

For the central galaxy stellar masses (Table 1), we first find the galaxy center by taking all stellar resolution elements within $0.3\,R_{\rm vir}$ of the halo center, then recalculating the shrinking spheres center using only this stellar mass. We then measure the stellar mass within $0.1\,R_{\rm vir}$ of the galaxy center.

2.5. Ion Abundance Calculation

As mentioned above, we use the Ploeckinger & Schaye (2020b) tables to calculate the ion fractions. We assume no dust depletion as dust is expected to be sputtered at the temperatures we are interested in (e.g., Tsai & Mathews 1995). These use the same photoionizing UV/X-ray background as assumed for the

[6] One minor difference is that the m12f and m12i halos were simulated using a code update (Wetzel et al. 2023, Section 2.4.1). The effect of this difference should be minimal.

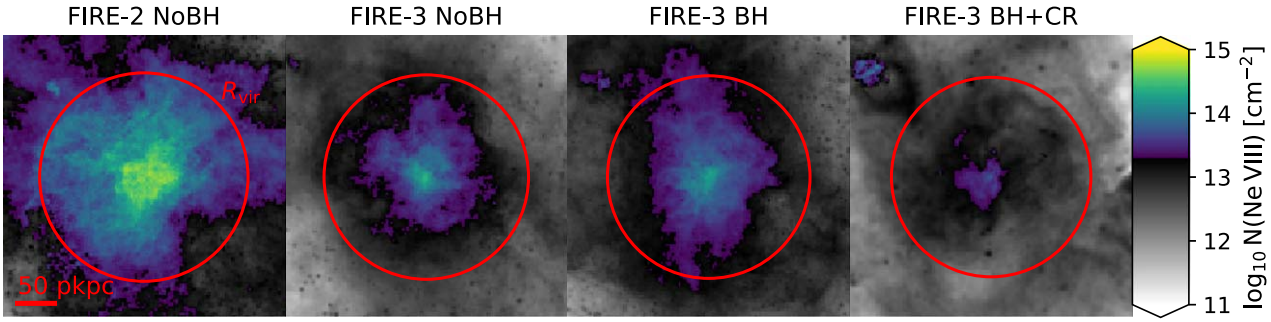

Figure 1. Ne VIII column density images for the m12f halo at $z = 1$ ($M_{vir} \approx 10^{11.8}\,M_\odot$), simulated with four different physics models (different panels). The color scale switches from black and white to colors at a column density of $10^{13.3}$ cm^{-2}, which is the minimum detectable column density in Burchett et al. (2019; CASBaH survey). Qu et al. (2024; CUBS survey) have a higher detection limit, $\approx 10^{14}$ cm^{-2}. The different panels show the same physical area; the red circles show each halo's virial radius. The panels illustrate the observably different Ne VIII column densities produced by the different FIRE physics models.

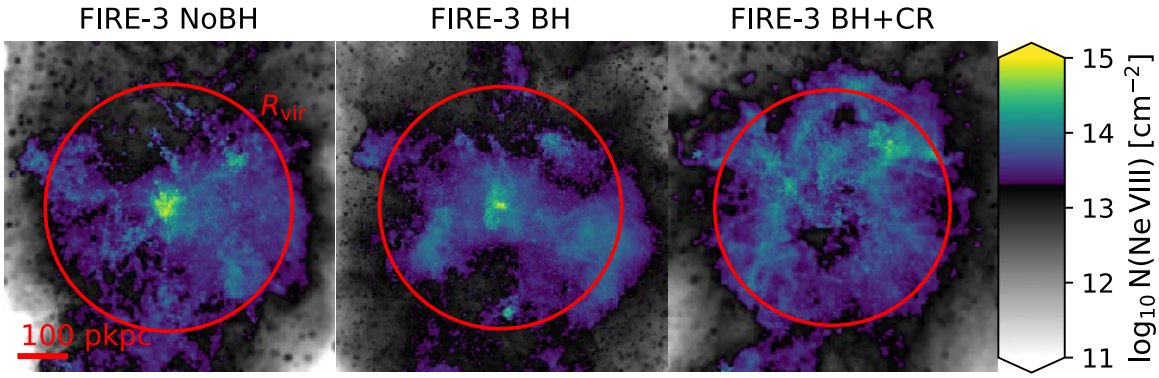

Figure 2. As Figure 1, but for the m13h113 halo (also at $z = 1$, $M_{vir} \approx 10^{12.7}\,M_\odot$) run with the three FIRE-3 physics models. The Ne VIII in m13 halos has a clumpier distribution than in the m12 halos. This is because Ne VIII ion fractions are low at the virial temperatures of these halos, meaning the ion preferentially traces somewhat cooler, denser, clumpier gas than the volume-filling phase (see also Figures 3 and 4).

radiative cooling in the FIRE-3 simulations we study. For consistency, we use these same tables for our FIRE-2 analysis. We interpolate these tables (linearly for ion fraction and redshift, and linearly in log space for temperature, density, and metallicity) to calculate ion fractions for a given resolution element.

2.6. Column Density Calculation

Given the number of ions in each resolution element, we now want to calculate the column density along various lines of sight. We do this by creating "column density maps." We first define a volume and a line-of-sight direction. For the volume, we use a cube with side lengths (diameter) of $4\,R_{vir}$, centered on the halo center. For the line-of-sight directions, we simply use the x-, y-, and z-axes of the simulation. We note that these directions are random with respect to the galaxy and halo orientation.

We divide the plane perpendicular to the line of sight into pixels of size $(3\,\mathrm{pkpc})^2$. We then distribute the ions in each resolution element in the volume across these pixels based on each resolution element's position and size. This size is the MFM smoothing length. We assume the ion distribution in each resolution element is described by a spherical Wendland C2 kernel (Wendland 1995). Figures 1 and 2 show examples of these column density maps.

3. Ne VIII in FIRE

3.1. Column Densities and Clumpiness

We start our analysis by considering how Ne VIII is distributed in the FIRE halos. To do this, we show images of some representative examples of m12 and m13 halos in Figures 1 and 2, respectively. For each halo mass sample, we show one halo, simulated using the different labeled physics models. These plots show the simulations at $z = 1.0$, with the line of sight along the z-axis. All column densities are measured to $2\,R_{vir}$ in either direction along the line of sight from the halo center.

Comparing the m12 and m13 halos, the Ne VIII in the m12 halos is fairly smoothly distributed, while this ion has a clumpier distribution in the m13 halos. Differences between the panels for the different physics models reflect some broader differences, but some of these differences are just a coincidence for these halos and this particular redshift.

For the m12 halos, the FIRE-2 NoBH model generally predicts higher column densities than the FIRE-3 models analyzed here, and the FIRE-3 NoBH and BH models predict similar column density profiles across halos and redshifts. The FIRE-3 BH+CR model generally predicts lower column densities than the other two FIRE-3 models, but with only two halos for this physics model, this is somewhat uncertain. In general, the FIRE-3 NoBH and BH models also predict similar column densities in m13 halos, while FIRE-3 BH+CR predicts lower column densities in the halo center. Note that the "hole" in the center of the m13h113 FIRE-3 BH+CR image is not a common feature in the m13 BH+CR model.

We explore the clumpiness of the m12 and m13 halos in more detail in Figure 3. We show all the halos from our sample, and highlight the halos and redshift from Figures 1 and 2 in black. We measure the volume-weighted Ne VIII "smoothness"

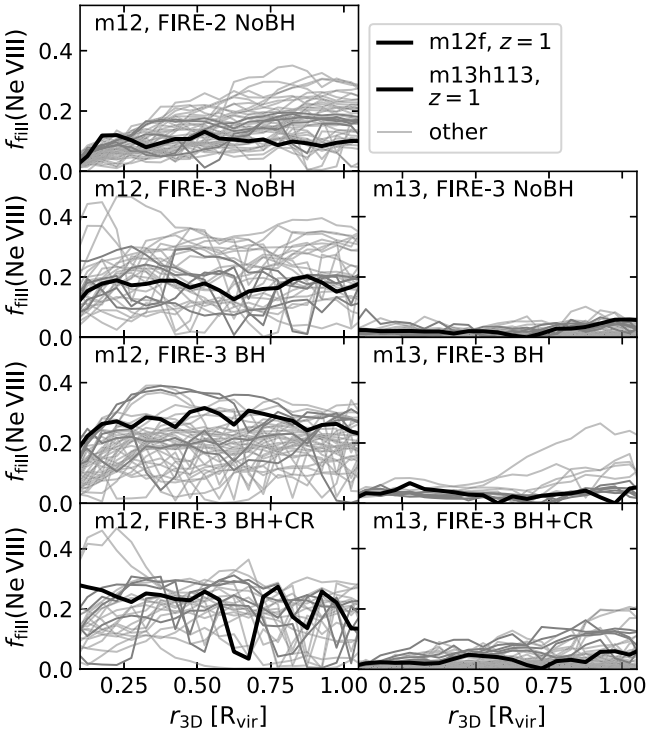

Figure 3. Filling fraction of Ne VIII in the m12 and m13 halos at redshifts 0.5, 0.6, 0.7, 0.8, 0.9, and 1.0 with different physics models (different panels). We calculate the filling fraction as the volume-weighted Ne VIII number density, divided by the Ne VIII-weighted Ne VIII number density (this is the inverse of the clumping factor in Equation (1)). Values lie between 0 and 1; higher values mean the distribution is smoother. The black curves show the halos from Figures 1 and 2. The Ne VIII distribution in the m13 halos is typically clumpier than that in m12 halos. This is because the Ne VIII ion fraction peaks roughly at the temperature of the volume-filling gas in the m12 halos, but this ion traces cooler, denser gas than the volume-filling phase in the hotter m13 halos.

using the clumping factor

$$f_{\rm c,\,V} = \frac{\langle n({\rm Ne}^{7+})^2\rangle_V}{\langle n({\rm Ne}^{7+})\rangle_V^2} = \frac{\langle n({\rm Ne}^{7+})\rangle_{\mathcal{N}({\rm Ne}^{7+})}}{\langle n({\rm Ne}^{7+})\rangle_V}, \quad (1)$$

where the angle brackets indicate averages over resolution elements, weighted by volume V or number of Ne VIII ions $\mathcal{N}(\mathrm{Ne}^{7+})$. We indicate the Ne VIII number density as $n(\mathrm{Ne}^{7+})$. The second equality shows that $f_{c,V}$ is equal to the Ne VIII-weighted Ne VIII density divided by the volume-weighted Ne VIII density.

In order to keep our range of values limited (between 0 and 1), we show $f_{\rm fill} = 1/f_{c,V}$ in Figure 3. We note that this can be interpreted as the fraction of the CGM volume occupied by Ne VIII in a simple case: if some fraction of the resolution elements all have the same ion density $n_{\rm Ne\ VIII}$, and the rest contain no Ne VIII, $1/f_{c,V}$ is the fraction of the volume which contains Ne VIII ions.

We calculate $f_{\rm fill}$ in radial bins of size 0.05 $R_{\rm vir}$ and show the smoothness as a function of (3D) distance to the halo center. We restrict this analysis to radial bins because the halos are significantly denser in their centers than in their outskirts. A clumping factor measured over the whole halo would therefore not only be sensitive to how smoothly the Ne VIII is distributed, but also to how concentrated the ions are in the halo center.

As suggested by the maps in Figures 1 and 2, the Ne VIII in the m12 halos is more smoothly distributed than in the m13 halos. A similar plot to Figure 3 showing the volume-weighted gas density clumping factor shows that the m13 CGM is not intrinsically clumpier than the m12 CGM, meaning that the differences here are a result of how well (or poorly) Ne VIII probes the smooth, virialized gas in the halo.

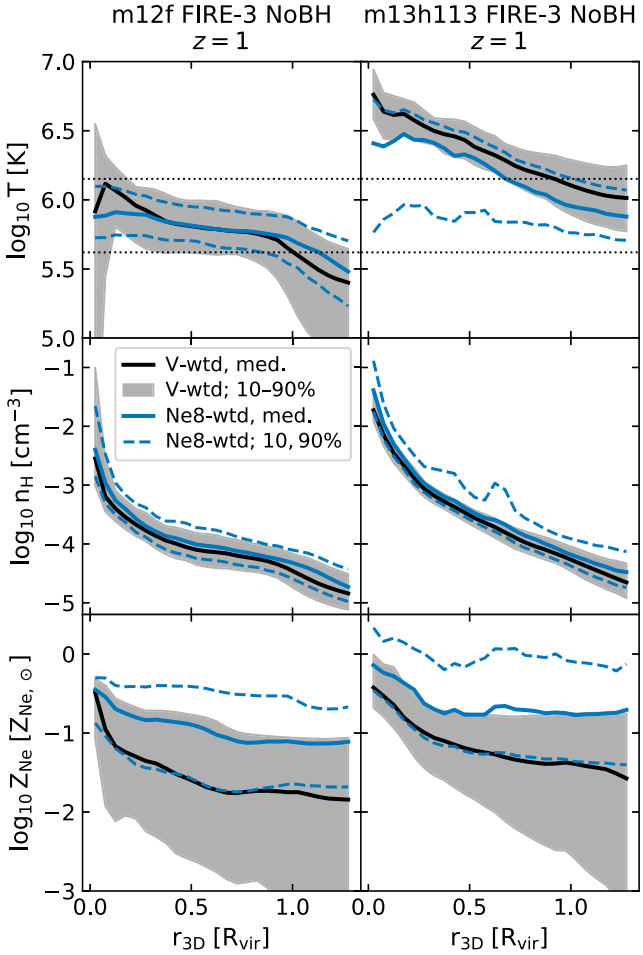

Figure 4. Temperature, density, and neon abundance profiles for the m12f FIRE-3 NoBH halo and the m13h113 FIRE-3 NoBH halo, both at $z = 1$. These halos are shown in the second panel from the left in Figure 1 and the left-hand panel in Figure 2, respectively. Blue curves show Ne VIII-weighted medians (solid lines) and the 10th and 90th percentiles of the Ne VIII-weighted distributions. Black curves and shading show the same percentiles of the volume-weighted distributions. The dotted horizontal lines in the top panels show the range of temperatures where, for gas in CIE, the Ne VIII ion fraction is at least 0.1 times the maximum ion fraction in CIE.

3.2. Ne VIII and CGM Properties

In Figure 4, we explore the temperature, density, and metallicity of the Ne VIII in the CGM.[7] We consider how Ne VIII traces the warm-hot CGM in these halos, and whether the ionization of the neon is driven primarily by electron collisions or by photoionization.

In the top panels of Figure 4, we show the volume- and Ne VIII-weighted temperature of an example m12 (left) and m13 (right) halo. We show the FIRE-3 NoBH model for the m12f and m13h113 halos at $z = 1$; these halos are also shown in Figures 1 and 2. The volume-weighted median and 10th–90th percentile temperatures (black) are shown in these top panels. The gas in the higher-mass m13 halos, is, as expected,

[7] We normalize the neon mass fraction by the Asplund et al. (2009) neon solar mass fraction $10^{-2.90}$ here, following Ploeckinger & Schaye (2020b).

hotter than the gas in the m12 halos. In the blue lines, we show the same percentiles of the Ne VIII-weighted temperature distribution. In the m12 halos, the Ne VIII traces roughly the same temperatures as the volume-filling gas phase. In the m13 halos, Ne VIII preferentially traces gas that is cooler than the volume-filling phase, although some Ne VIII is found in the volume-filling gas.

The horizontal dotted lines indicate why. For gas in CIE, these indicate the temperature range where the Ne VIII fraction is at least 0.1 times the maximum ionization fraction in CIE. In the m13 halos, Ne VIII makes up a relatively small fraction of the neon in the volume-filling phase, especially in the halo center. Though there is less gas at temperatures where the Ne VIII fraction is high, what gas there is contains relatively many Ne VIII ions. In the m12 halos, the volume-filling, virialized gas is at temperatures close to that where the Ne VIII fraction reaches its maximum, so this ion traces that volume-filling gas well.

In the middle panels of Figure 4, we show the volume- and Ne VIII-weighted density percentiles in these same halos. In the m12 halos, the Ne VIII traces the density of the volume-filling gas quite well, with only a slight bias to higher densities. This bias toward high densities is stronger in the m13 halos. This is in line with the clumpier Ne VIII distribution in m13 halos relative to the m12 halos.

Finally, we show the same distributions for metallicity (neon mass fraction) in the bottom panels of Figure 4. Unsurprisingly, the Ne VIII preferentially traces neon-enriched gas. Though different halos and physics models have different metallicity profiles, the median Ne VIII-weighted metallicity consistently lies roughly along the 90th percentile of the volume-weighted metallicity profile.

The top panels show that much of the Ne VIII in both the m12 and m13 halos is at temperatures where Ne VIII can be found in CIE. (For m13 halos, a lot of the Ne VIII is at temperatures above the CIE peak, but collisional ionization also dominates over photoionization in this regime.) However, some gas around $R_{\rm vir}$ in some m12 halos is photoionized, and gas outside $R_{\rm vir}$ in m12 halos is typically photoionized. Additionally, some of the CIE-temperature gas has low densities, where photoionization affects the fraction of neon in the Ne^{7+} ionization state. This occurs in m12 halos and in the outskirts of m13 halos. In other words, much of the Ne VIII in m12 halos, and in the outskirts of m13 halos, is not clearly in photoionization equilibrium (PIE) or CIE, but instead ionized by both photons and electrons. In both m12 and m13 halos, the gas closer to the halo center is densest, and most likely to be in CIE, while the lower-density gas near $R_{\rm vir}$ is most likely to be photoionized.

3.3. What Determines the CGM Ne VIII Content?

We have seen that Ne VIII broadly traces warm-hot gas in the CGM, and is a good tracer of the volume-filling gas in $M_{\rm vir} \sim 10^{12}\,M_\odot$ halos. Now we explore which CGM properties determine the Ne VIII content of the halos most strongly. We focus on the m12 halos here since we this is where most of the observational constraints are (see Section 4).

In the top-left panel of Figure 5, we show the average Ne VIII column densities in the halos simulated with the different physics models. We calculated these by dividing the number of Ne VIII ions with a (3D) distance to the central galaxy between 0.1 and 1 $R_{\rm vir}$ by $\pi\,R_{\rm vir}^2$. This illustrates the magnitude of the

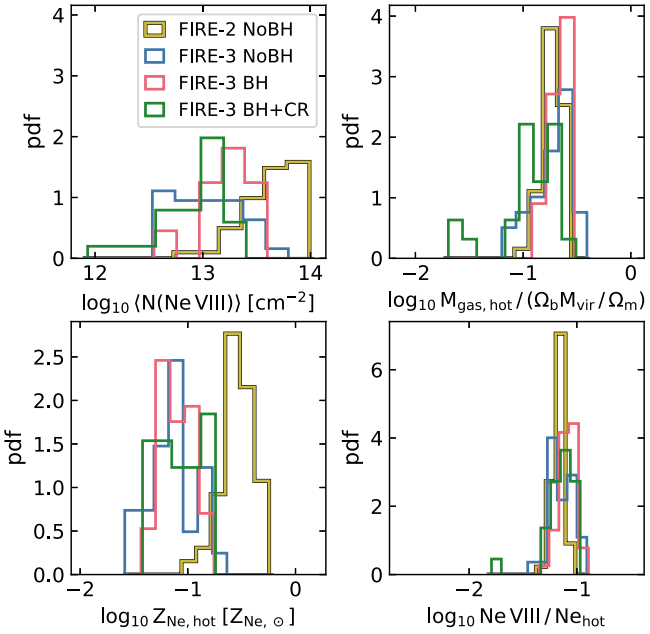

Figure 5. Histograms of various CGM properties determining the Ne VIII content of m12 halos. Different colors show different physics models. For each physics model, the histograms show probability density functions calculated over each halo run with that physics model, including data at redshifts 0.5, 0.6, 0.7, 0.8, 0.9, and 1.0 for each halo. The top-left panel shows the mean CGM Ne VIII column density. As shown in Figure 1, the FIRE-2 NoBH mean column densities are higher than those of the FIRE-3 models. The top-right panel shows the hot ($>10^5$ K) gas mass between 0.1 and 1 $R_{\rm vir}$, normalized to the halo baryon budget. The bottom-left panel shows the mass-weighted metallicity of the ($>10^5$ K) gas between 0.1 and 1 $R_{\rm vir}$. The FIRE-2 NoBH model has a markedly higher metallicity than the FIRE-3 models, and the difference is large enough to explain the column density differences. The bottom-right panel shows the Ne VIII ion mass between 0.1 and 1 $R_{\rm vir}$, divided by the $T > 10^5$ K neon mass in that same radial range. Note that for the FIRE-3 BH+CR model, we only have two halos available.

column density differences we want to explain. The clearest difference is between the FIRE-2 NoBH model, and the three FIRE-3 models: the FIRE-2 model predicts higher Ne VIII column densities than the FIRE-3 models (see also Figure 1).

In the top-right panel, we show histograms of the warm-hot ($>10^5$ K) CGM gas mass, normalized to the halo baryon budget, for our m12 sample. We find warm-hot CGM masses of roughly 0.1–0.3 times the halo baryon budget. The warm-hot CGM mass distributions for the different physics models are similar.

In the bottom-left panel of Figure 5, we compare the (mass-weighted mean) metallicity of the warm-hot CGM ($>10^5$ K, 0.1–1 $R_{\rm vir}$) in our different physics models. Here, we see clear differences: the FIRE-2 NoBH simulations, with the highest Ne VIII column densities, also have clearly higher metallicities than the FIRE-3 models. The differences are of the right size to explain the column density differences.

Finally, in the bottom-right panel of Figure 5, we check the Ne VIII ion fractions: the fraction of neon ions in the Ne VIII ionization state. Note this is, at most, 0.24 in CIE. We specifically compare the Ne VIII mass to the warm-hot neon mass: we divide all Ne VIII at 0.1–1 $R_{\rm vir}$ by the neon at 0.1–1 $R_{\rm vir}$ and $T > 10^5$ K. We have checked that most Ne VIII is at temperatures $>10^5$ K, so we are essentially measuring the Ne VIII ion fraction in the warm-hot gas phase. We see a slightly lower Ne VIII fraction in the FIRE-2 NoBH model, compared to the FIRE-3 models. The differences are, however,

small compared to the metallicity and column density differences between the models.

We conclude that the Ne VIII column densities are higher in the FIRE-2 simulations than in the FIRE-3 simulations due to the higher metallicity of the FIRE-2 NoBH warm-hot CGM in the halos we considered. We have checked that the neon abundance differences reflect the total metallicity differences between the models. The different models also include halos with a similar $M_{\rm vir}$ distribution, except that the two FIRE-3 BH +CR halos are at the higher end of the $M_{\rm vir}$ distribution.

The (neon) metallicity differences are in part due to the ≈0.3 dex lower neon yields in the FIRE-3 simulations, compared to FIRE-2 (see Section 2.2). However, this is not enough of a change to fully explain the differences. The FIRE-3 models additionally produce m12 central galaxies with lower stellar masses than the FIRE-2 simulations at fixed halo mass. Lower stellar masses also mean lower metal production, and therefore, a lower halo metal budget. In Appendix B, we show that FIRE-3 NoBH halos with higher halo masses, and stellar masses comparable to those of the FIRE-2 NoBH halos, still produce lower Ne VIII column densities than those FIRE-2 NoBH halos.

4. Comparison to Ne VIII Observations

4.1. How to Compare Observed and Simulated Halos

4.1.1. The CASBaH Data

We compare our FIRE predictions for Ne VIII column densities to the observations of Burchett et al. (2019). Specifically, we use some of the quantities in their Table 1. Briefly, their data combines a set of absorption spectra, which they searched for Ne VIII absorption, with the CASBaH galaxy catalog (Prochaska et al. 2019). This catalog includes galaxy spectroscopic redshifts, and galaxy stellar masses determined with spectral energy distribution (SED) fits and those redshifts.

These galaxies are matched to Ne VIII absorption systems found along the sightline based on impact parameter (<450 pkpc) and velocity difference (<500 km s^{-1}).[8] They select the closest galaxy to the line of sight if there are different options.

For galaxies without corresponding absorbers, a 3σ upper limit on the Ne VIII column density was determined. That means we can treat this as a survey where any sightline passing close enough to a galaxy was searched for absorption by that galaxy's halo. Therefore, medians and percentiles of the column densities around halos at a given impact parameter are a good comparison for the measurements and upper limits in the data.

4.1.2. The CUBS Data

We also compare our Ne VIII column densities to the observations of Qu et al. (2024). Their analysis is part of the CUBS survey (Chen et al. 2020). Qu et al. (2024) searched for Ne VIII absorption at redshifts $0.43 \lesssim z \lesssim 0.72$ in quasar spectra, and compiled a catalog of galaxies close to their quasar sightlines. The CUBS and CASBaH quasar sightline samples do not overlap (Burchett et al. 2019; Chen et al. 2020), meaning the two data sets are independent of each other.

Qu et al. (2024) determined their galaxy redshifts spectroscopically. Stellar masses were calculated based on three photometric bands. The relation Qu et al. (2024) used for this was fitted to a calibration sample of galaxies, with stellar masses derived from SED fits. Scatter in the fitted relation causes an estimated systematic error in the stellar masses of ≈0.2 dex. Qu et al. (2024) calculate halo masses $M_{\rm 200c}$ from their stellar masses.[9]

Galaxies were matched to absorbers in two steps. First, all galaxies within within 3 $R_{\rm 200c}$ of the sightline were selected. Galaxies were then grouped if they were within 1 Mpc and 500 km s^{-1} of each other. Second, absorbers were matched to (groups of) galaxies if they had a velocity separation $\leqslant$1000 km s^{-1}. For galaxies and groups without measured column densities, 2σ upper limits on the Ne VIII column densities were determined. Within groups, a single galaxy is selected as the absorber counterpart. Based on correlations with O VI absorption, Qu et al. (2024) chose the galaxy with the smallest impact parameter in units of $R_{\rm 200c}$ as the counterpart.

Qu et al. (2024) compared their data to the CASBaH Ne VIII data. They examined the CASBaH absorbers, and flagged five of them as being significantly contaminated by interlopers. These interlopers are other absorption lines at other redshifts, which overlap with the reported Ne VIII absorption lines. Specifically, the difference is in the treatment of absorption systems with significant contamination in one of the Ne VIII 770, 780 Å doublet components. Burchett et al. (2019) consider the candidate absorption systems to be detections, based in part on the other absorption lines detected at the same redshift as the candidate Ne VIII. Qu et al. (2024) instead treat these as upper limits, based on a more conservative detection criterion where both doublet lines must be more clearly identified.

In their further analysis, Qu et al. (2024) treat the "flagged" measurements from Burchett et al. (2019) as upper limits in order to get a sample with consistent detection criteria. We will indicate these data points with open symbols in our plots. Conversely, some of the 2σ upper limits in the CUBS data might have been considered detections at a similar column density by Burchett et al. (2019). In this work, we do not attempt to resolve the observational question of exactly how robust the flagged detections are. Instead, below we consider how our main conclusions depend on whether they are treated as detections versus upper limits. As we will see, our overall conclusions regarding the median profiles are largely unaffected, though the quantitative degree by which the simulations underpredict the scatter is increased if all the Burchett et al. (2019) detections are assumed to be robust.

4.1.3. Halo Masses

Our goal is to compare the FIRE CGM to the CGM observations of Burchett et al. (2019) and Qu et al. (2024). The Burchett et al. (2019) observations are of Ne VIII CGM absorbers around isolated galaxies with stellar masses of $\sim 10^9$–$10^{11}\,M_\odot$. For CGM comparisons to observations, matching the halo masses is important, because the halo mass determines the CGM baryon budget, extent, and virial temperature, i.e., three important factors determining the ion content of the warm-hot phase. Burchett et al. (2019) measured the stellar masses of their galaxies, and used a modified version

[8] Burchett et al. (2019) grouped individual absorbers into absorption systems if they were within ≈600 km s^{-1} of each other. The redshift attributed to the absorption system is its central velocity.

[9] The halo mass $M_{\rm 200c}$ and its radius $R_{\rm 200c}$ are defined such that the mean density in the halo is 200 times the critical density at the halo redshift.

(Burchett et al. 2016) of a function fit to abundance-matching simulations (Moster et al. 2013) to obtain halo masses based on these stellar masses.

Burchett et al. (2019) do not, however, report errors on the halo masses. Since there is substantial scatter in the SMHM relation, these could be quite large. Therefore, we used a UniverseMachine stellar and halo mass catalog (Behroozi et al. 2019) to reconstruct the SMHM relation and look into some sources of errors.[10] Specifically, we used the catalogs based on the Small MultiDark-Planck (SMDPL) dark-matter-only simulation (Klypin et al. 2016; Rodríguez-Puebla et al. 2016), which has a volume of $(0.4\,\mathrm{Gpc}/h)^3$. Behroozi et al. (2019) analyzed these using the ROCKSTAR halo finder (Behroozi et al. 2013a) and CONSISTENT TREES Behroozi et al. (2013b) merger trees. We only used UniverseMachine galaxies flagged as centrals for this analysis. From this catalog, we estimate the true halo mass probability distribution given an observed galaxy stellar mass and redshift. We do this by finding the distribution of halo masses in the catalog for a given stellar mass, and then combine that with the probabilities of different true stellar masses from the observations.

This different method makes a difference for the inferred most likely halo masses (i.e., those with the highest probability density), which is quite large for central galaxies with stellar masses $\gtrsim 10^{10.5}\,M_\odot$. Accounting for scatter in the SMHM relation also leads to larger uncertainty estimates, again mostly at $M_\star \gtrsim 10^{10.5}\,M_\odot$. We give a more detailed explanation of our method, and our recommendations for how to estimate these halo masses, in Appendix A.

Qu et al. (2024) did determine their halo masses using an SMHM relation from Behroozi et al. (2019). However, they use an overdensity of 200 relative to the critical density to define halos, where we use the Bryan & Norman (1998) density definition, and they do not report errors on their halo masses. We therefore apply the same method as described above to the CUBS stellar masses to calculate the most likely halo mass, and its errors, as we applied to the CASBaH data.

4.2. Column Density Profiles

In Figure 6, we show the masses (Bryan & Norman 1998 definition) and redshifts of the halos in our simulated sample, and the observed samples of Burchett et al. (2019, CASBaH) and Qu et al. (2024, CUBS). The black lines indicate the masses and redshifts of different halos. If a halo was simulated with different physics models, we only show the masses and redshifts for one of them. This is for legibility, and is reasonable because the halo masses differ little between these simulations with different physics models. For the observed data points, we show the most likely halo masses (mode of the probability density function) with points. The 1σ uncertainty ranges show the log halo mass range enclosing a probability of 68%.

We only show data points with impact parameters $<$450 pkpc in Figure 6. For the CASBaH data, this matched their own galaxy selection, but this excludes some of the CUBS upper limits, especially at high halo masses. We focus on these impact parameters because, for the m12 halos, this 450 pkpc is $\approx$2–3 $R_{\rm vir}$, which is toward the edge of the zoom-in region of the simulations. For the m13 halos, larger impact parameters might be acceptable given the volume of the zoom region, but the CUBS upper limits there are not very constraining, so we focus on the impact parameters where Ne VIII was detected.

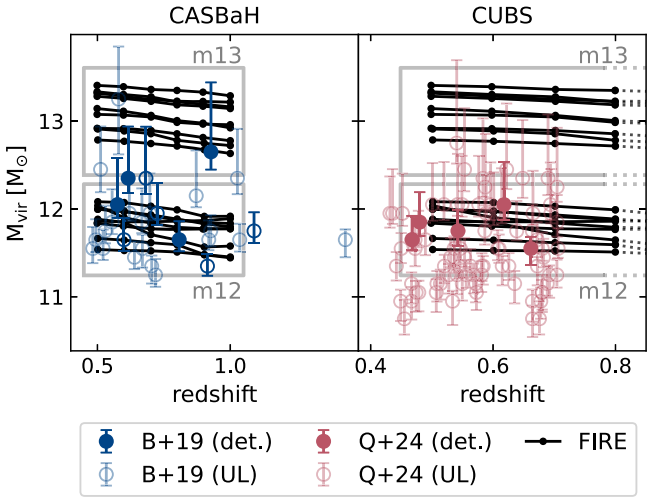

Figure 6. Halo masses and redshifts for the simulated halos (black lines), compared to the distribution of halo masses and redshifts of the galaxies Burchett et al. (2019, left, B+19; CASBaH survey) and Qu et al. (2024, right, Q+24; CUBS survey) found within 450 physical kpc of their quasar sightlines. We calculate the observed galaxy halo masses as described in Section 4.1. Filled points indicate detections (det.), while lighter-colored open points are upper limits (UL). Darker-colored open points indicate CASBaH Ne VIII detections that do not meet the stricter Qu et al. (2024) detection criteria. The points show the halo mass with the highest probability, and error bars show the 1σ uncertainties. The boxes indicate the ranges of mass and redshift where we consider data points good matches to the m12 and m13 halo samples.

The gray boxes are drawn at the minimum and maximum halo mass and redshift in the m12 and m13 samples, with a redshift margin of 0.05, and a log halo mass margin of 0.2. An observed galaxy is considered a good match to the m12 or m13 FIRE sample if its best-estimate halo mass and redshift fall within the solid box. In Figures 7 and 8, these halos are shown with black markers. We will also compare FIRE predictions to data points in larger sections of this plot, using larger margins of 0.1 in redshift and 0.4 in log halo mass. We consider data points in these larger regions to be plausible matches. In Figures 7 and 8, these halos are shown with gray markers. These margins for the most likely halo masses are fairly consistent with whether the halo mass uncertainties include the simulated ranges.

In Figures 7 and 8, we compare the m12 and m13 halo column densities in the FIRE-2/3 simulations to the measurements of Burchett et al. (2019) and Qu et al. (2024). For all physics models and for the m12 and m13 halos, the median column densities are consistent with the observed upper limits. Though some upper limits lie below the median curves, at least about half the upper limits and measurements lie above the median curves in all physics models we consider, in both the m12 and m13 halos. However, the median and 90th percentile profiles for all models underpredict the highest reported column density values.

For the FIRE-3 m12 halos, the observed (non-upper-limit) column densities are mostly above the 90th percentile of the simulated values at the same impact parameter. For the FIRE-3 models, overall more than 10% of the observed column densities in the CUBS and CASBaH data (including sufficiently tight upper limits) within $\sim$0.5–1 $R_{\rm vir}$ lie above the 90th percentile of the simulation predictions. Because most

[10] https://halos.as.arizona.edu/UniverseMachine/DR1/SMDPL_SFR/ (Accessed: 2023 June 15).

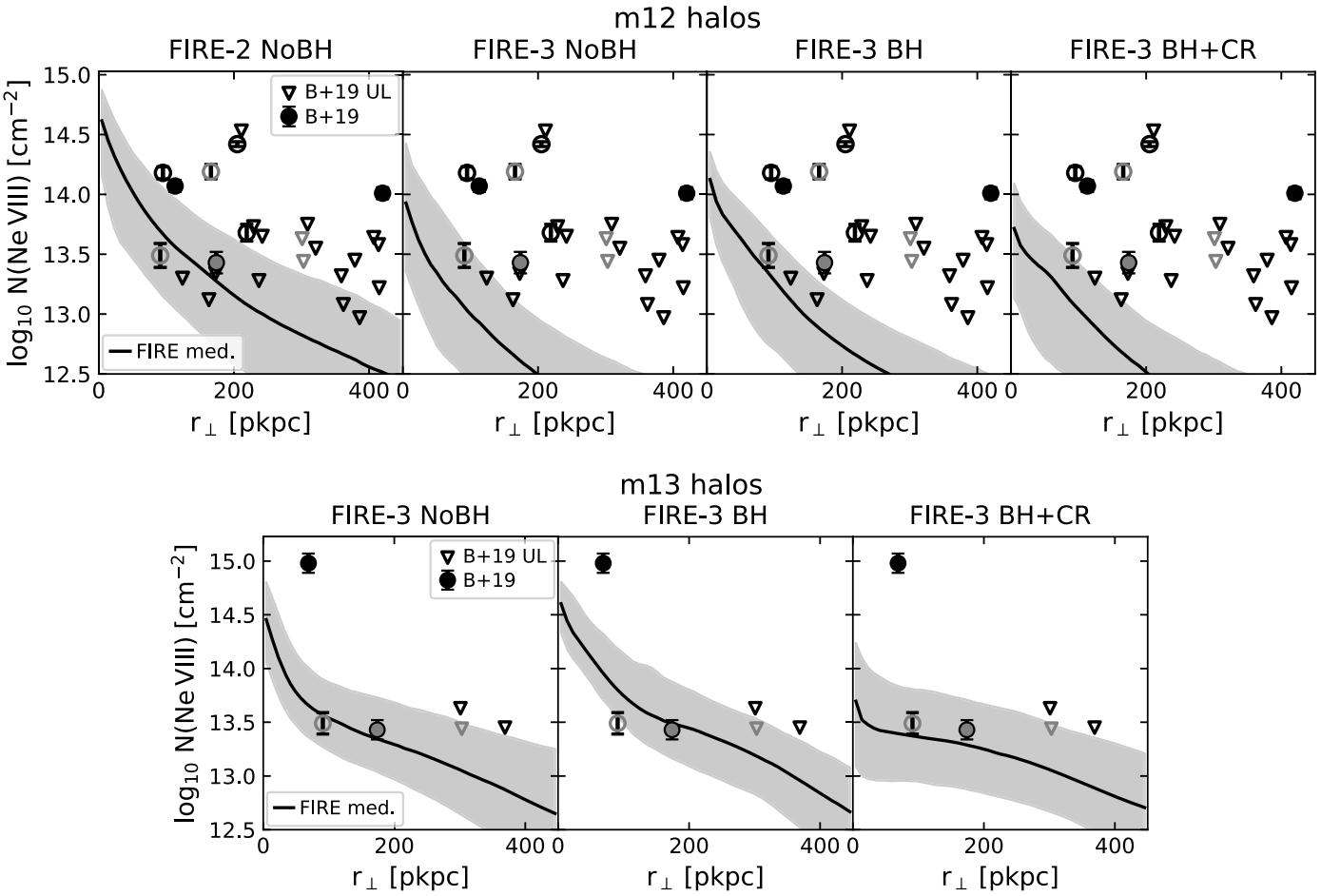

Figure 7. Ne VIII column densities predicted from our simulations, compared to the values (points with 1σ error bars) and upper limits (3σ, open triangles) found by Burchett et al. (2019, B+19) in the CASBaH survey. The black points show observed galaxies that match the m12 (top panels) and m13 (bottom panels) halo mass and redshift range well, and gray points show plausible matches (see the text for the precise selections). Open circles indicate CASBaH Ne VIII detections that do not meet the stricter Qu et al. (2024) detection criteria; Qu et al. (2024) treat these measurements as upper limits. For the simulation data, solid lines show median column densities as a function of the impact parameter, while the shaded region shows the 10th–90th percentile range of the column density at a given impact parameter. Different panels show different physics models, indicated above each panel. The m12 FIRE-2 NoBH model medians are consistent with the data, i.e., the median lies above $\lesssim$50% of the detections and upper limits. The data do not allow for much higher median column densities than this model predicts within $\approx$200 kpc. We note that some of these highest values exceed groups of upper limits at similar impact parameters and halo masses. However, the FIRE-2 NoBH model may underpredict the highest measured values, depending on how we interpret the open circles. All three m12 FIRE-3 models underpredict the measured values. The m13 halos match two of the observed column densities, but underpredict the largest measured value.

observations are upper limits, we cannot rule out the lower median column densities predicted by these models, but it is clear that these FIRE-3 models do not produce enough high Ne VIII column densities in m12 halos to match the detections.

The FIRE-3 m13 halos match the two measured Burchett et al. (2019) column densities that plausibly match the m13 halo mass range, but all models underpredict the column density of the one measurement that clearly matches the m13 halo mass range (the one with Ne VIII column $\approx 10^{15}$ cm^{-2}, which is the highest measured value in the Burchett et al. 2019 sample).

Overall, the FIRE-2 NoBH simulations match the observations better than the FIRE-3 simulations. We show a more detailed comparison of the FIRE-2 halos with observations in Figure 9. The left panel compares the simulations to the data from Burchett et al. (2019) only, the middle panel to the data from Qu et al. (2024) only, and the right panel to the combined data set. In that figure, we quantify the comparison between the FIRE-2 simulations and observations further by estimating conservative upper limits on the median and 90th percentile of Ne VIII column densities as a function of the impact parameter (dark gray curves). We do this by calculating percentiles from the measurements and upper limits together, treating all upper limits as actual detections at the highest column densities allowed. Although the treatment is simple, it is instructive because it quantifies how high the observed profile percentiles can be in the most optimistic case. This exercise also allows us to assess the impact of treating the detections from Burchett et al. (2019) that did not meet the stricter Qu et al. (2024) detection criteria (see Section 4.1.2) as detections versus upper limits.

More specifically, we calculate running percentiles. We order the data by impact parameter, then take the first n points, and calculate the desired percentile of their column densities and the median of their impact parameters. This is the first point on the upper limit curve. We add points by taking the same percentiles of data points 1 through $n+1$, 2 through $n+2$, etc. For these calculations, we used all data points shown in each panel, i.e., data that matches the simulated halo mass range well and reasonably. We chose the number of points n to use for each data set and percentile by looking for values that

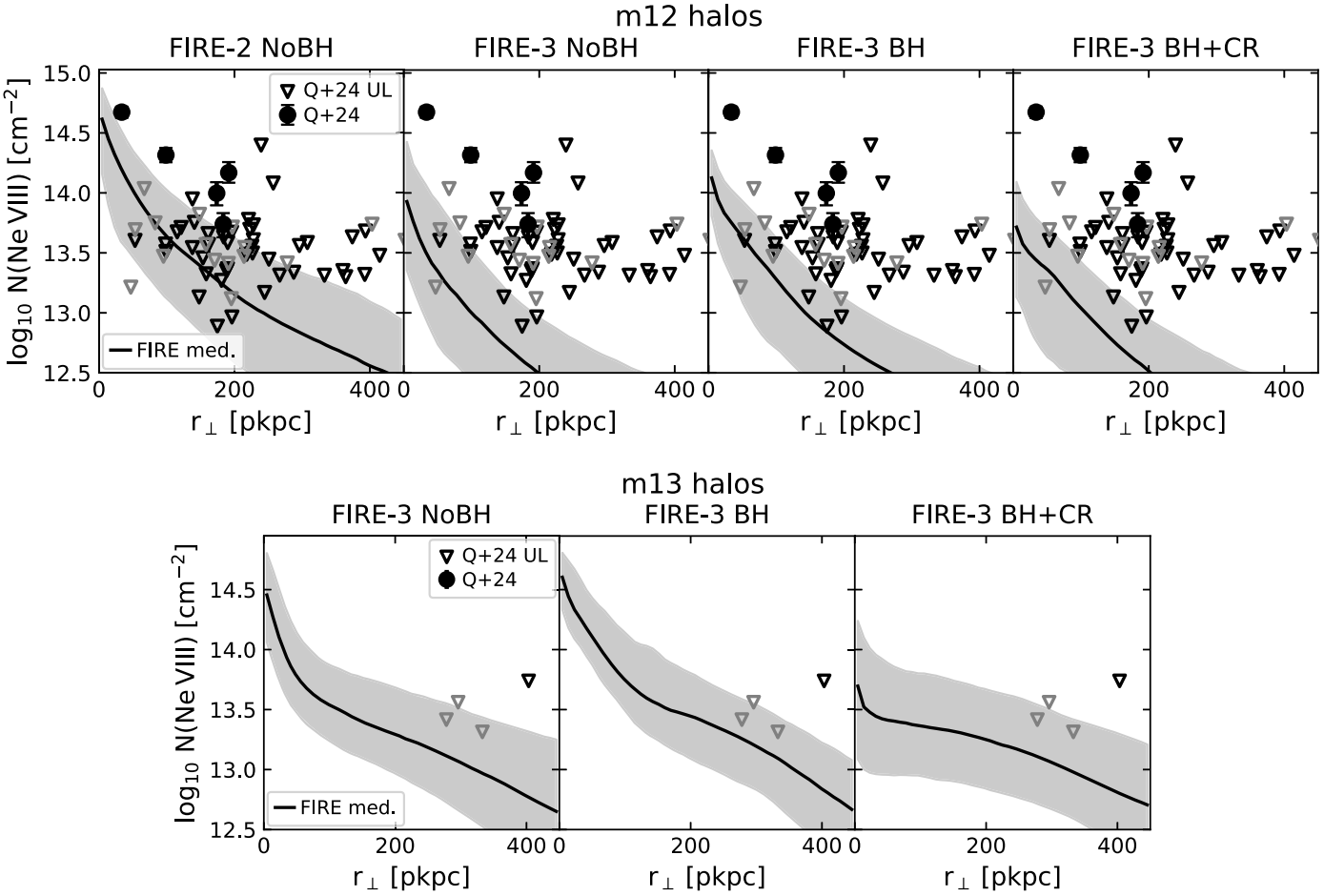

Figure 8. As Figure 7, but comparing the m12 (top row) and m13 (bottom row) halos to the Qu et al. (2024, Q+24) CUBS survey observations. The error bars on their measurements and their upper limits are both 2σ. Again, the FIRE-2 NoBH m12 medians are consistent with the data, and about as large as the data allow within ≈100 kpc. The FIRE-3 models underpredict the highest measured column densities. The m13 halos are consistent with the measured upper limits.

produced reasonably smooth curves, without sacrificing too much of the impact parameter range represented in the data.

From this, we draw the following conclusions:

1. In the inner impact parameter bins, where the observations are most constraining as this is where we expect the highest columns, the conservative upper limits to the observed medians are similar to the predicted medians from FIRE-2 for the m12 halos. Therefore, the true median profile cannot be significantly higher than predicted by FIRE-2. This is so regardless of whether we consider only the data from Burchett et al. (2019), only the data from Qu et al. (2024), or the combined data set. Furthermore, this conclusion holds independent of whether all the detections reported by Burchett et al. (2019), including the ones that did not meet the stricter detection criteria of Qu et al. (2024), are robust or best interpreted as upper limits.
2. If we focus on the Burchett et al. (2019) data, the innermost running median point from the CASBaH data in Figure 9 is calculated from five column densities reported as detections by the authors, plus three upper limits that lie below the five detections. Therefore, the estimated "upper limit" on the running median in that region is actually a direct estimate of the median itself. This indicates that if all the detections reported by Burchett et al. (2019) are robust, the true median column densities cannot be substantially lower than the FIRE-2 predictions at impact parameter ≈150 kpc. Thus, the FIRE-2 simulations analyzed predict a median Ne VIII column density profile consistent with the observations at that impact parameter. This also means that if the FIRE-2 model underpredicts the 90th percentile column density profile, it is the column density scatter that is underestimated, not the median.
3. Focusing on the estimated upper limits to the 90th percentiles, the conclusions depend more sensitively on whether we use the Burchett et al. (2019) versus the Qu et al. (2024) data. For the Qu et al. (2024) data in the middle panel, we see that in the inner halo, the upper limit to the 90th percentile is similar to the 90th percentile from FIRE-2. This suggests that the FIRE-2 simulations may be entirely consistent with the CUBS data for the Ne VIII column density profile, including its scatter. For the Burchett et al. (2019) data, the 90th percentile upper limits are higher due to the high column detections. If all the reported detections are assumed to be robust, the data imply that while FIRE-2 predicts a consistent median profile, the simulations significantly underestimate the scatter of the distribution.

5. Analytical Modeling

Some of the Burchett et al. (2019) and Qu et al. (2024) column densities are higher than predicted in any of our FIRE

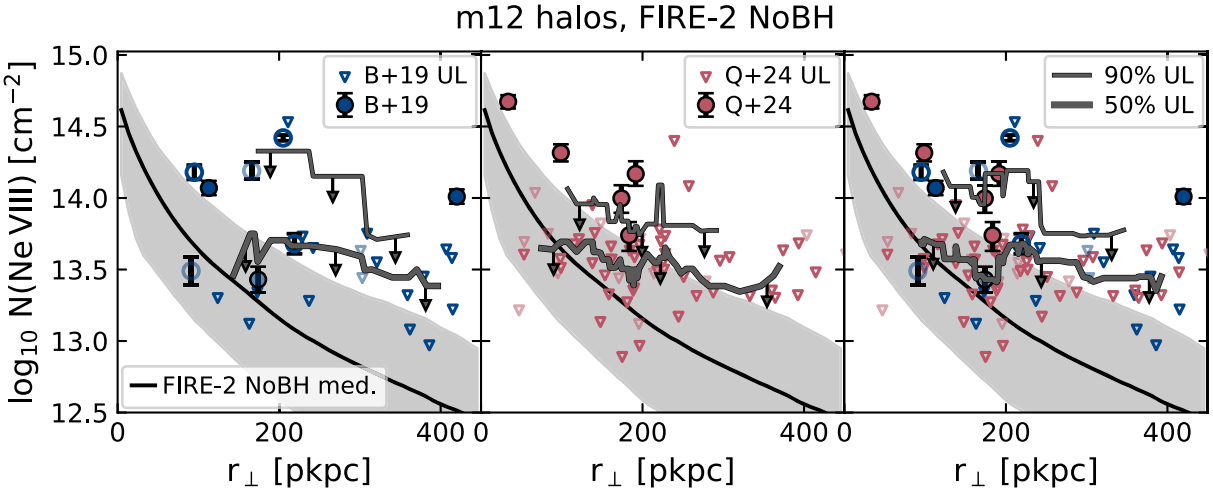

Figure 9. As in Figures 7 and 8, but focusing on the FIRE-2 NoBH m12 halos and estimating upper limits to the median and 90th percentile profiles. The left-hand panel compares the CASBaH (Burchett et al. 2019) Ne VIII column density measurements (circles) and 3σ upper limits (triangles) as a function of impact parameter to the median (solid, black line) and 10th–90th percentile range (gray shaded area) predicted from our FIRE-2 NoBH m12 simulations. Open/filled and lighter/darker symbols have the same meaning as in Figure 7. The middle panel shows the same as the left-hand panel, but instead of the CASBaH data, we show the CUBS data (Qu et al. 2024) with 2σ upper limits. In the right-hand panel, we show both data sets together. We estimate conservative upper limits on the median and 90th percentile of the observed column densities as a function of impact parameter in each panel (see the text in Section 4.2 for details). We show these running percentiles of the measured column densities and upper limits with the dark gray lines. From left to right, we use 8 (15), 10 (20), and 15 (30) points to calculate the running median (90th percentile).

simulations. Some of these, such as the $\approx 10^{14}$ cm^{-2} absorption system at an impact parameter of ≈400 pkpc, might be outliers or mismatched with their galaxies: This data point lies above many upper limits at smaller impact parameters. However, the simulations may also be imperfect models.

To better understand the halo properties needed to explain the observed Ne VIII column densities, we predict column densities using a simple analytical model. The goals here are (i) to see how we expect the column densities to depend on the halo mass, size, and temperature, and (ii) to check whether the high Burchett et al. (2019) and Qu et al. (2024) column densities can be explained with reasonable CGM masses and metallicities.

In our phenomenological model, derived in more detail in Appendix C, we assume the various thermodynamical properties of the halo gas are power-law functions of distance to the halo center. We describe the gravitational potential as

$$v_c \propto r^m, \tag{2}$$

where v_c is the circular velocity, r is the distance to the halo center, and m is an exponent to be determined. We additionally try a few different values of the entropy profile logarithmic slope:

$$l \equiv \frac{d \ln K}{d \ln r}, \tag{3}$$

where K is the entropy $K = kTn^{-2/3}$, k is the Boltzmann constant, and n is the total free particle number density.

We also assume hydrostatic equilibrium, yielding a power-law temperature profile $T \propto r^{2\,m}$, with a normalization depending on l, m, and v_c at the virial radius: $v_c(R_{vir}) = \sqrt{\frac{G\,M_{vir}}{R_{vir}}}$. The implied density profile is $n_H \propto r^{-\frac{3}{2}l+3m}$, and we set the normalization in the fiducial model by requiring that the mass of this CGM gas is the cosmic baryon fraction of the halo mass M_{vir} (at 0.1–1 R_{vir}).

Assuming the warm-hot CGM contains the cosmic baryon fraction of the halo in mass is an optimistic (but not extreme) assumption. However, we want to explore an optimistic model here to assess the consistency of the high-column-density measurements with the cosmic baryon budget. We will also explore lower values of $f_{CGM} = M_{CGM}/(\Omega_b\, M_{vir}/\Omega_m)$, where M_{CGM} is the (warm-hot) CGM mass between 0.1 and 1 R_{vir}.

In calculating the column densities for these profiles, we assume a metallicity of $0.3\,Z_\odot$ in our fiducial model. We calculate ion fractions using the Ploeckinger & Schaye (2020b) ionization tables, in the same way as for the FIRE predictions.

Next, we need to decide on a circular velocity profile slope m. We base these choices on the v_c slopes in Navarro–Frenk–White (NFW) halo mass profiles (Navarro et al. 1997). In these profiles, the circular velocity profile slope $\frac{d \log v_c}{d \log r}$ depends on $\frac{r}{r_s}$, where r_s is a scale radius. We roughly estimate the relation between r_s and R_{vir} using Table 3 of Dutton & Macciò (2014); this yields concentrations $R_{vir}/r_s \approx 6$–9 for halos with $M_{vir} = 10^{11.5}$–$10^{13.5}\,M_\odot$ around redshifts 0.5 and 1, decreasing with halo mass. This yields slopes $\frac{d \log v_c}{d \log r} \approx -0.2$ to 0.25 in the radial range 0.1–1 R_{vir}. The slopes decrease (become more negative) with halo center distance and increase (become more positive) with halo mass. We choose a fiducial circular velocity slope $m = -0.1$, which is reasonable for the large radii (in virial radius units) where many of the measurements most likely lie.

For the entropy slopes, we show a range of plausible values. Zhu et al. (2021) find outer halo entropy slopes ≈1.2 from an observational group/cluster sample. Babyk et al. (2018) study entropy profiles in halos over a range of masses, using observations around early-type galaxies and clusters. At small radii, their findings are consistent with a slope of two-thirds, and at larger radii with 1.1. An entropy slope of zero can occur in, for example, cluster centers (e.g., Donahue et al. 2006). Although the halo mass range relevant for Ne VIII observations is mostly below groups and clusters, we note that an entropy slope ≈1 is representative of cooling flow models for Milky

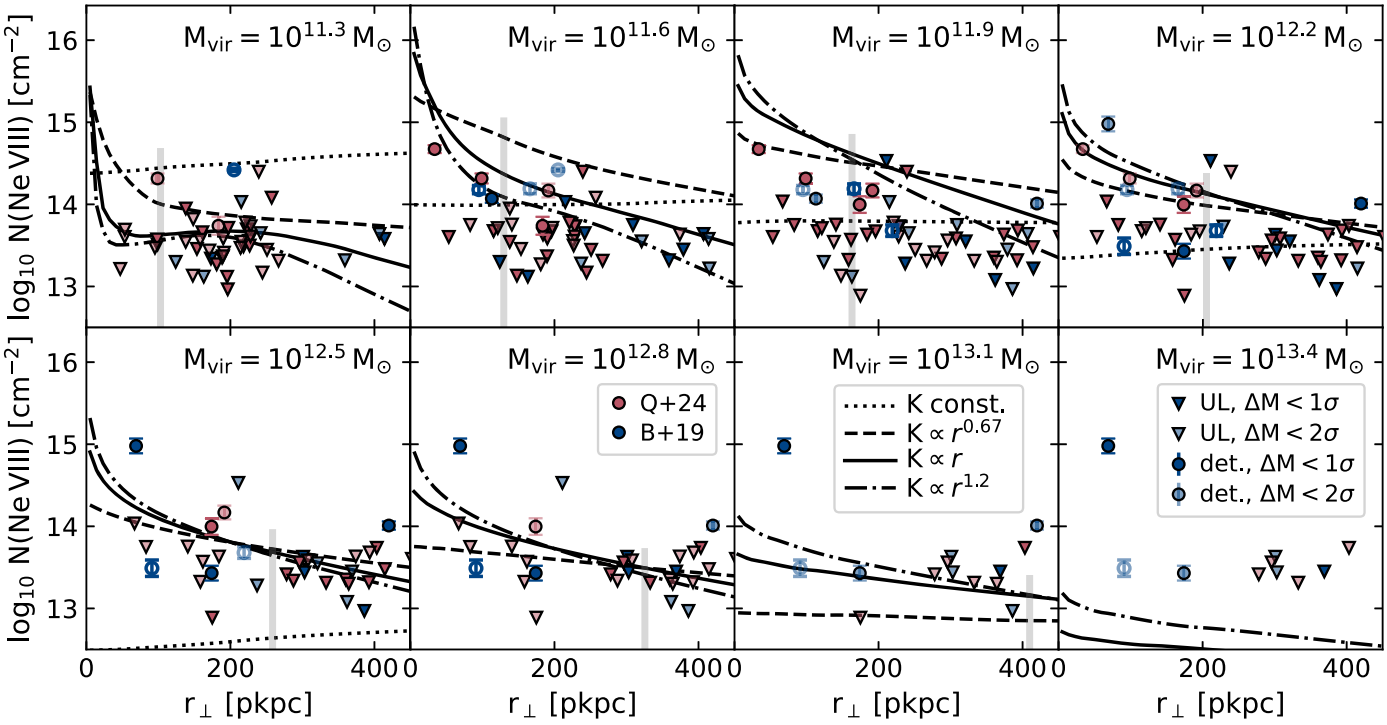

Figure 10. Ne VIII column density as a function of impact parameter for some power-law CGM models with a warm-hot CGM mass budget $f_{\rm CGM} = 1$ and a uniform metallicity of 0.3 $Z_\odot$. Different logarithmic entropy slopes are shown in different line styles. We use a circular velocity slope $m = -0.1$ (Equation (2)). Each panel shows one halo mass, indicated in the upper right of the panel. We show how the measurements (points with error bars) and upper limits (downward-facing triangles) of Burchett et al. (2019, blue; CASBaH) and Qu et al. (2024, red; CUBS) compare to these models. The brighter measurement and upper limit points have halo masses within 1σ of the halo mass shown in the panel, while points with lighter colors have halo masses between 1σ and 2σ from the model halo masses. The open blue circles indicate CASBaH Ne VIII detections that do not meet the more conservative detection criteria of Qu et al. (2024). Vertical gray lines indicate the virial radius; for $M_{\rm vir} = 10^{13.4}\,M_\odot$, this radius is outside the plotted range. All measurements but one are achievable in some variation of a power-law model with a baryonically closed CGM and a uniform metallicity of $Z = 0.3\,Z_\odot$, and many upper limits require lower CGM gas fractions and/or metallicities.

Way-mass halos (Stern et al. 2019; Sultan et al. 2024, in preparation). We show this slope as well.

We note that not all entropy and circular velocity profile combinations are possible. If both slopes are zero, there is no pressure gradient, the assumption of hydrostatic equilibrium becomes meaningless, and the temperature profile normalization is not constrained. If l is too large and/or m is too negative, the density slope becomes too steep and the mass integral within the virial radius diverges.

We show these model Ne VIII profiles in Figure 10, alongside the observations. We note that the upper limits are 2σ for Qu et al. (2024, CUBS, red) and 3σ for Burchett et al. (2019, CASBaH, blue). All measured column densities but one can be achieved in a power-law CGM model, containing the cosmic baryon fraction of the halo mass in the warm-hot CGM phase, and with a uniform metallicity of 0.3 $Z_\odot$. Though this is a somewhat optimistic model, it does not require unphysical CGM gas masses or extreme CGM metallicities. We note that the validity of these power-law models beyond $R_{\rm vir}$ is uncertain.

We also note that the halos producing the highest column densities are within (though at the high end of) the m12 mass range (see Figure 6), meaning these halos are represented in our simulation sample.

In Figure 11, we further explore these power-law models in relation to the measured column densities. We choose the halo mass from Figure 10 consistent with the most data points, $M_{\rm vir} = 10^{12.2}\,M_\odot$, and explore whether the data are consistent with lower CGM mass fractions than the cosmic baryon fraction of Figure 10.

We see that some data points are indeed consistent with lower CGM masses of $\sim 0.3\Omega_{\rm b}/\Omega_{\rm m}\,M_{\rm vir}$, although we note that we are still assuming a constant metallicity of 0.3 times solar throughout the halo. Metallicity and CGM mass are not precisely degenerate in this column density model, as the CGM mass (along with the chosen entropy and circular velocity slopes) determines the density profile. Lower densities can affect the ionization balance if they are low enough for photoionization to become important. In practice, though, a model with CGM mass $0.3\Omega_{\rm b}/\Omega_{\rm m}\,M_{\rm vir}$ and solar metallicity looks similar to the model with CGM mass $\Omega_{\rm b}/\Omega_{\rm m}\,M_{\rm vir}$ and 0.3 times solar metallicity shown in blue in Figure 11. The largest differences are furthest from the halo center and with the steepest entropy slope.

However, some data points can only be explained with this power-law model of the volume-filling phase if $f_{\rm CGM} \times (Z\,/\,Z_\odot) \approx 0.3$, and if the entropy slope is steep. This implies that these high measured column densities might be probing baryon-complete halos, or perhaps particularly dense or metal-enriched warm-hot gas within a halo. The highest measured column density can only be explained with a relatively high CGM metallicity or a nonuniform metallicity or density distribution. We expect Ne VIII to broadly trace the volume-filling gas in a halo of the mass in Figure 11, but Figures 1 and 3 show that some denser-than-average Ne VIII can exist in these halos.

The metallicities and CGM warm-hot gas content in the FIRE halos (Figure 5) paint a similar picture to our analytical model: the FIRE-2 NoBH model has halo metallicities $\sim$0.3 times solar, and $f_{\rm CGM}$ parameters in the $\approx$0.1–0.3 range. As the

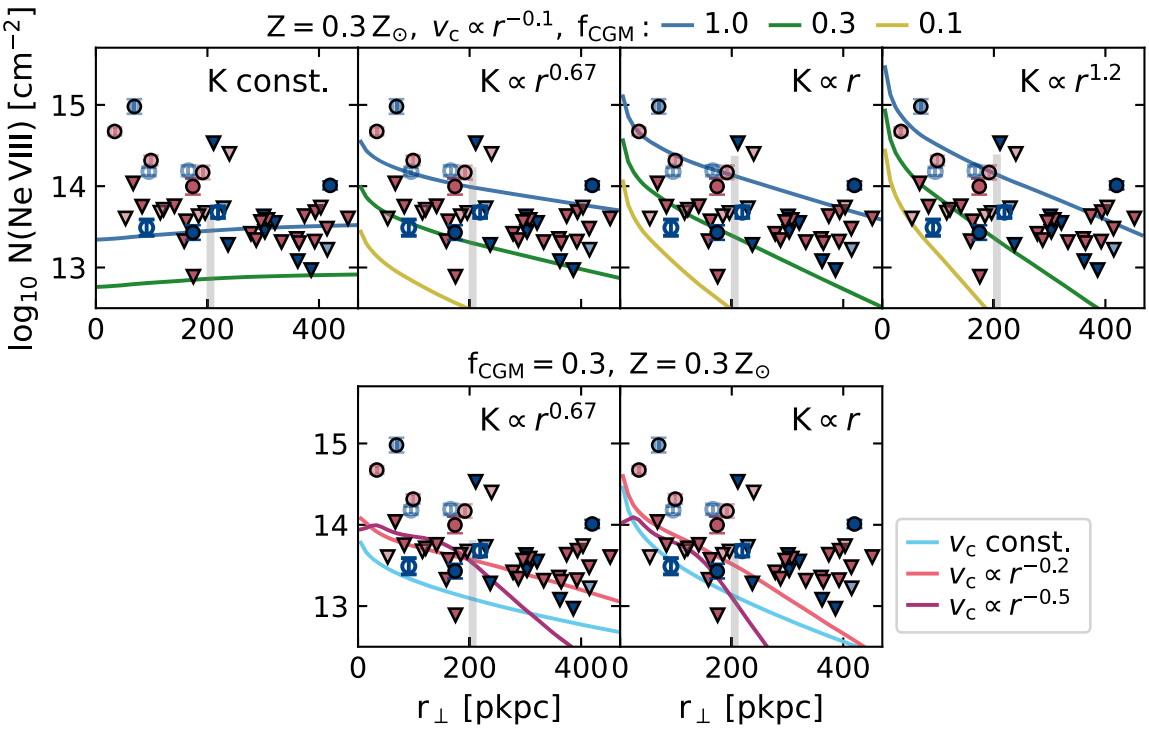

Figure 11. Top row: a comparison of analytical models with different CGM baryon fractions $f_{\rm CGM} = M_{\rm CGM}/(\Omega_{\rm b}\, M_{\rm vir}/\Omega_{\rm m})$, where $M_{\rm CGM}$ is the (warm-hot) CGM mass. We show power-law models with different entropy slopes for a halo with $M_{\rm vir} = 10^{12.2}\, M_\odot$ and a metallicity of 0.3 $Z_\odot$ at redshift $z = 0.75$. Different entropy slopes are shown in different panels and slope values are given in the upper right of each plot. Model column densities are shown for $f_{\rm CGM} = 1$, 0.3, and 0.1. The measurements are shown in the same way as Figure 10, and vertical gray lines indicate the virial radius. While the data generally favor $f_{\rm CGM} \times (Z/Z_\odot) \approx 0.1$ ($f_{\rm CGM} \approx 0.3$ for the $Z \approx 0.3\, Z_\odot$ assumed in the figure), some measurements are only consistent with our power-law model with $f_{\rm CGM} \times (Z/Z_\odot) \approx 0.3$ ($f_{\rm CGM} \approx 1$ in the figure), and a high entropy slope. Bottom row: for two entropy slopes, we show the effect of varying the circular velocity profile slope. The differences between the profiles are generally smaller than those over the plausible range of entropy slopes.

analytical models would suggest, these halos are consistent with the upper limits, but the 90th percentile of the simulated column densities lies below the largest measured values. Note that these large measured values might represent high column density values within typical halos, rather than halos with uniformly high densities and metallicities.

The m12 halos simulated with the FIRE-3 models have similar $f_{\rm CGM}$ to the FIRE-2 NoBH model, but they have metallicities around and below ≈0.1 times solar. They indeed produce lower column densities than the FIRE-2 NoBH halos, and their median column densities are consistent with the upper limits, but lie below all the measured column densities. As discussed in Sections 2.2 and 3.2, the lower metallicities in the FIRE-3 halos analyzed here are likely due to the lower metal yields in FIRE-3, and the lower stellar masses at fixed halo mass resulting from the enhanced SN momentum injected in converging flows in the FIRE-3 runs included in this work.

The CASBaH data allow higher warm-hot CGM metal masses than the CUBS data. Although the CASBaH and CUBS upper limits on the median column density are similar, the CASBaH data imply higher 90th percentile column densities within $R_{\rm vir}$ than the CUBS data allow. As the amount of Ne VIII in the halo sets the mean column density, rather than the median, the higher 90th percentiles are relevant here.

The Ne VIII data broadly favor CGM mass and metal contents $f_{\rm CGM} \times (Z/Z_\odot) \sim 0.1$ for $\sim 10^{12}\, M_\odot$ halos. We have checked that the implied total metal masses are consistent with being produced by nucleosynthesis from observed stars. Below we compare the Ne VIII result with constraints from other observations on the CGM mass and metallicity.

The Milky Way hot CGM gas fraction is difficult to constrain, because X-ray absorption- and emission-line measurements are mostly sensitive to gas in the inner ≈50 kpc, as are the dispersion measures toward LMC pulsars. Indeed, redshift 0 X-ray absorption in extragalactic sources may come from hot ISM rather than circumgalactic gas (Yao & Wang 2005). However, Bregman et al. (2018) favor $f_{\rm CGM} \sim 0.1$–0.2 based on constraints on the density profile slope, and they find metallicities $Z \gtrsim 0.3\, Z_\odot$ within ≈50 kpc. Miller & Bregman (2015) found similar $f_{\rm CGM}$ and metallicities $Z = 0.3$–$1\, Z_\odot$ from O VII and O VIII absorption and emission. Gupta et al. (2012) have also used O VII and O VIII absorption and emission lines to constrain the Milky Way hot CGM mass. Assuming a uniform hot CGM mass density (i.e., a flat density profile), they found higher values of $f_{\rm CGM} > 0.5$ at $Z = 0.3 Z_\odot$. In their review, Donahue & Voit (2022) give a Milky Way value of $f_{\rm CGM} \lesssim 0.5$ from X-ray absorption and emission, while observations of ram pressure stripping of Milky Way satellite galaxies favor similar or larger electron densities (their Figure 10).

For external galaxies, Bregman et al. (2022) constrained warm-hot CGM gas masses by stacking observations of the thermal SZ effect around 12 nearby L_* galaxies. They found $f_{\rm CGM} \approx 0.3$ for their default assumed gas temperature. Their $f_{\rm CGM}$ is consistent with our findings, although we do not claim to meaningfully constrain $f_{\rm CGM}$ or metallicity separately. Zhang et al. (2024) measure X-ray emission from the CGM by stacking eROSITA data around galaxies in bins of stellar mass. Their measurements are sensitive to $f_{\rm CGM}$ and metallicity, and they find values of $f_{\rm CGM} \times (Z/Z_\odot) \approx 0.03$–0.15 for roughly

Milky Way-mass galaxies with different metallicity assumptions, and a larger statistical error range (their Figure 9). Larger values than 0.15 are allowed if the hot gas temperature is lower than they assumed.

Overall, measuring the hot metal or gas mass in the Milky Way and other L_* galaxies is difficult, and comes with systematic uncertainties from assumptions necessary in the analysis. Nonetheless, the values implied by most other observations than those of Ne VIII absorption are similar to those we estimate here.

6. Discussion

6.1. FIRE Column Densities versus Observations

We have compared various FIRE simulations of $\sim 10^{12}\,M_\odot$ (m12) and $\sim 10^{13}\,M_\odot$ (m13) halos at $z = 0.5$–1.0 to observations of CGM Ne VIII absorbers by Burchett et al. (2019, CASBaH) and Qu et al. (2024, CUBS). For the m12 halos, we find that the FIRE-2 NoBH model produces higher Ne VIII column densities in the CGM than the three FIRE-3 models we examine, including one that similarly has no AGN feedback. This is largely due to the higher CGM metallicity in the FIRE-2 halos. The FIRE-2 predictions for the median m12 Ne VIII column densities are consistent with the data, but the 90th percentile of the column densities as a function of impact parameter is lower than the CASBaH data imply, and tentatively lower than the CUBS data imply. The FIRE-3 m12 halo Ne VIII column densities underpredict the data more systematically. For the m13 halos, the data is limited, but the FIRE predictions are mostly consistent with the data available.

Overall, within the FIRE samples we analyzed, the m12 FIRE-2 NoBH model reproduces the Ne VIII observations better than the FIRE-3 models. As we discuss in Appendix B, differences in central galaxy stellar masses contribute to these differences. Generally, the FIRE-2 m12 halos have higher stellar masses than FIRE-3 halos with the same halo mass, as discussed in the previous section. The higher stellar masses and the higher stellar metal yields (per unit stellar mass) in FIRE-2 result in higher CGM metallicities.

In Section 5 we analyzed idealized, power-law analytic models of the CGM to gain further insight into the physical conditions required to explain the observed Ne VIII columns. Using this analytic framework, we found that the observations favor models with a product of the halo gas fraction and metallicity of roughly $f_{\rm CGM} \times (Z\,/\,Z_\odot) \sim 0.1$. Reassuringly, this is consistent with the FIRE-2 m12 halos, which we find to be the best match to the observations in the simulation sample, as well as with independent empirical constraints, including X-ray observations.

There are some caveats to our comparison with observations. The small sample sizes (in both FIRE halos and measured absorbers) imply significant statistical uncertainties. Furthermore, the large uncertainties in some of the observed galaxies' halo masses and the lack of "contamination" from nearby halos and/or intergalactic medium in the FIRE zoom regions introduce some systematic uncertainties in the comparisons of zoom-in simulations with observations.

There are also some purely observational uncertainties. Notably, the Ne VIII 770, 780 Å doublet falls in a crowded part of the spectrum (e.g., Burchett et al. 2019; see Figure 6). This makes it more difficult to measure the equivalent width and line width of an absorber, and even to identify the doublet. This might explain some of the differences between the Qu et al. (2024) and Burchett et al. (2019) data: within 450 pkpc of galaxies, Burchett et al. (2019) measure column densities $\geqslant 10^{14}\,{\rm cm}^{-2}$ in six out of 28 sightlines, while Qu et al. (2024) measure absorption of this strength in three out of 65 sightlines. (We excluded sightlines with column density upper limits $\geqslant 10^{14}\,{\rm cm}^{-2}$ from our counts.) These are small numbers, impacted by, for example, a Qu et al. (2024) absorber with a Ne VIII column density barely below $10^{14}\,{\rm cm}^{-2}$. However, the incidence of high-column-density CGM absorbers is clearly higher in the Burchett et al. (2019) data.

Finally, we note that the highest observed column density we compare to is $\approx 10^{15}\,{\rm cm}^{-2}$, measured by Burchett et al. (2019) and most consistent with an m13 host halo. Tripp et al. (2011) had previously measured this absorption system; it consists of many absorption components, some of which have large velocity offsets from the host galaxy or group: $\approx$200–400 km s^{-1} (e.g., Burchett et al. 2019, bottom two panels of the rightmost column in Figure 2). Tripp et al. (2011) concluded that Ne VIII was tracing an outflow in this system. In principle, FIRE simulations include galaxy/halo-scale outflows. However, if such systems are rare, it is reasonable that our set of halos did not capture an outflow event like this.

6.2. Can Cool Gas Cause the Observed Ne VIII Absorption?

In this paper, we have presented evidence that the Ne VIII absorption profiles observed around $z \lesssim 1$ galaxies are generally well explained by a volume-filling, hot phase. Here, we briefly comment on the alternate possibility that the Ne VIII absorption instead arises in a cool ($T \sim 10^4$ K) phase. This scenario was addressed by Burchett et al. (2019), who concluded this is unlikely for the bulk of the observed Ne VIII on CGM scales. The reason is that Ne VIII cannot be produced by collisional ionization in cool gas, so it would have to be photoionized. However, for Ne VIII to be produced by photoionization by the cosmic UV/X-ray background, the hydrogen densities must be very low since the Ne VIII fraction peaks at $n_{\rm H} \lesssim 10^{-5}\,{\rm cm}^{-3}$ for photoionized gas. There are two issues with this. The first is that, in order to explain the observed columns, the path lengths $L = N_{\rm H}/n_{\rm H}$ must be comparable to (or larger than) the virial radius of the halos. The second is that these low densities are comparable to (or lower than) the densities in the hot phase, which is both predicted to exist and observed in X-rays in $\sim 10^{12}\,M_\odot$ halos (e.g., Figure 4). Since $P \propto nT$, this would imply not only that the cool phase be volume filling, but it would also be underpressurized by $\sim$100$\times$ relative to the $T \sim 10^6$ K phase. Outside the virialized CGM, i.e., at large impact parameters not yet heated by accretion shocks or feedback, some Ne VIII could arise from low-density, photoionized gas (e.g., Stern et al. 2018), but this cannot explain the main CGM observations considered in this paper. In summary, a cool phase interpretation has severe difficulties explaining the CGM observations. Local sources of ionization are unlikely to change this overall conclusion as their effects are typically limited to relatively small impact parameters (e.g., Upton Sanderbeck et al. 2018; Zhu & Springel 2024).

6.3. How Do Other Simulations Fare?

Here, we consider whether other simulations can produce Ne VIII column densities that match these observations.

Ji et al. (2020) had previously compared FIRE-2 simulations to the Burchett et al. (2019) data, focusing on differences between a model with CRs and one without them. They find the model without CRs agrees well with the Ne VIII observations, although their CR model reasonably matches Ne VIII as well, and compares better to observations of some other ion column densities. We find that the median column density of the FIRE-2 NoBH model is consistent with the data, but this model may underpredict the higher percentiles of the column density at a given impact parameter. We note that the comparisons are somewhat different. For example, Ji et al. (2020) use a single halo simulated with a different FIRE-2 physics model, assume a different UV/X-ray background, compare data in virial radius units, and show the mean column density while we plot the median.

Wijers et al. (2020) discuss Ne VIII column densities around halos of different masses in the EAGLE simulations (Crain et al. 2015; Schaye et al. 2015; McAlpine et al. 2016; The EAGLE team 2017). We compare the CUBS and CASBaH data in, for example, Figure 10 to their Figure C1, $z = 0.5$ column density profiles. This is the highest-redshift data in that paper. The median column densities in EAGLE are consistent with the Qu et al. (2024, CUBS) data (mostly upper limits), but the 90th percentile column density profile lies below many of the CUBS and CASBaH measurements. The discrepancy is larger at $M_{200c} = 10^{11.5}$–$10^{12.0}\,M_\odot$, and smaller at $M_{200c} \approx 10^{12.5}$–$10^{13.0}\,M_\odot$.

Liang et al. (2016) predict Ne VIII column densities from zoom-in simulations of an $\sim 10^{12}\,M_\odot$ halo using the RAMSES code, comparing different feedback prescriptions. The Ne VIII column densities are $\lesssim 10^{14}\,\mathrm{cm}^{-2}$ for the two models shown in their Figure 15. This is consistent with the CUBS upper limits, but the higher end of the column density distribution at a given impact parameter is underpredicted for both the Burchett et al. (2019) and Qu et al. (2024) measurements for that halo mass. In comparisons of other CGM absorption lines to data, they conclude that models that produce realistic galaxies do not necessarily predict a realistic CGM.

Ford et al. (2013) predict Ne VIII column densities from a smooth particle hydrodynamic simulation in a cosmological volume. This model produces reasonable $\lesssim L_*$ galaxy properties, including the redshift 0 stellar mass function. They show median column densities at impact parameters of 10, 100, and 1000 pkpc, for halos of 10^{11}, 10^{12}, and $10^{13}\,M_\odot$. The column densities do not exceed $\approx 10^{13}\,\mathrm{cm}^{-2}$ across these impact parameter and halo mass ranges, well below the measured values.

As part of the AGORA Collaboration, Strawn et al. (2024) recently compared the CGM properties of a halo that reaches a mass of $\sim 10^{12}\,M_\odot$ at redshift 0, simulated with many different codes. In their Figure 15, they show predicted Ne VIII column densities as a function of impact parameter. These are for redshift 1, which the ART-I, ENZO, GADGET-3, GEAR, and AREPO-T simulations reach. These simulations show a wide range of median and 16th and 84th percentile profiles. The ENZO simulation column density profile is similar to that of the FIRE-2 NoBH model, and ART-I predicts somewhat higher values, with a median closer to the FIRE-2 NoBH 90th percentile. The other simulations predict lower column densities. Therefore, this ENZO simulation might be consistent with the data, while ART-I is the only simulation to overpredict the median observed column density profile. However, we note that with a single simulated halo not carefully matched to the observational sample, these comparisons are highly uncertain.

In summary, some of the Ne VIII predictions from simulations we have found in the literature may match median column density profiles; the data mostly provide an upper limit on this median. However, many simulations have trouble producing the higher Ne VIII column density values from the CUBS and CASBaH surveys, similar to what we found for the FIRE-2 simulations. Comparing cosmological hydrodynamical simulations with CGM observations is particularly valuable as different models that produce realistic galaxy populations can differ significantly in their CGM predictions. For example, Davies et al. (2020) show that different simulations that produce realistic $z \approx 0$ galaxy populations can have meaningfully different CGM gas fractions at the $M_{vir} \sim 10^{12}\,M_\odot$ mass scale probed by Ne VIII.

6.4. How Do Idealized Models Compare to the Observations?

Next, we consider whether previously published idealized models for the CGM can produce Ne VIII column densities that match these observations.

We first estimate Ne VIII in the power-law cooling flow model described in Stern et al. (2019), in which the CGM mass is such that the inflow rate induced by radiative losses equals the SFR. In such inflows radiative losses are balanced by compressive heating, so the temperature remains $\approx T_{vir}$ down to the galaxy radius, and entropy increases roughly linearly with radius. We further assume $Z = 0.3 Z_\odot$, and SFRs equal the 16th–84th percentiles in the UniverseMachine catalogs for the appropriate halo mass. We find that at all halo masses, cooling flow solutions (not shown here for brevity) that assume median SFRs predict Ne VIII column density profiles consistent with the median column density profiles allowed by the upper limits. At $M_{vir} \approx 10^{11.5}$–$10^{12}\,M_\odot$ detected Ne VIII columns are consistent with predictions of cooling flow solutions with 84th percentile SFRs, while at higher halo masses Ne VIII detections are underpredicted, typically by a factor of 3–10. These results hold for different assumed circular velocity profiles ($v_c \propto r^0$, $r^{-0.1}$, or $r^{-0.2}$) and different assumed metallicities (0.1–1 $Z_\odot$). We conclude that at $\lesssim 10^{12}\,M_\odot$ Ne VIII observations are consistent with the hot CGM phase forming a cooling flow, while a different origin is required to explain Ne VIII detections at higher halo masses.

A number of other groups have predicted Ne VIII column densities from analytical models. For example, Faerman et al. (2022) combine CGM gas masses for $10^{12}\,M_\odot$ halos from the Santa Cruz semi-analytical model (SAM) with an analytical model for CGM density, metallicity, etc. profiles. They find a large range of CGM parameters in the SAM, and use Milky Way–like halos with $0.05 < f_{CGM} \lesssim 1$ and CGM metallicities ≈ 0.1–$2\,Z_\odot$. (They limit the total halo baryon mass, including the galaxy, to the halo baryon budget.) They predict column densities as seen from inside a galaxy (as would be measured for the Milky Way halo). They predict column densities of 0.4–$2 \times 10^{14}\,\mathrm{cm}^{-2}$, depending on the halo CGM mass fraction. This would translate to column densities of $10^{13.9}$–$10^{14.6}\,\mathrm{cm}^{-2}$ in sightlines through the halo center, increasing with gas fraction. Those values are plausibly consistent with the Burchett et al. (2019) and Qu et al. (2024) measurements, although most measurements consistent with this halo mass are at impact parameters $\gtrsim 0.5\,R_{vir}$.

Voit (2019) predicts Ne VIII column densities at an impact parameter of 50 pkpc, as a function of halo mass, for different variations of a precipitation-limited CGM model. These models give $f_{\rm CGM} \approx 0.1$–0.3. Depending on the exact model variation, these column densities reach $\approx 10^{14}$–$10^{14.5}\,{\rm cm}^{-2}$ in halos with $M_{\rm 200c} \approx 1$–$2 \times 10^{12}\,M_\odot$, with lower column densities at lower halo masses. These predictions are somewhat high compared to the observations at $\approx 10^{12}\,M_\odot$, though we note they assume the CGM at these masses has solar metallicity.

Qu & Bregman (2018) compare their analytical CGM model predictions to a different set of Ne VIII observations and find agreement. They find $f_{\rm CGM} \sim 0.05$ for a metallicity of $0.3\,Z_\odot$ in $\sim 10^{12}\,M_\odot$ halos. They predict column densities $\sim 10^{14}\,{\rm cm}^{-2}$ for halos with a mass $\sim 10^{12}\,M_\odot$, and column densities up to $\approx 2 \times 10^{14}\,{\rm cm}^{-2}$ outside 0.3 virial radii in the different variations of their model. This is roughly the range of the Burchett et al. (2019) observations, and about as high as the Qu et al. (2024) data allow for the median column density.

7. Conclusions

We have predicted Ne VIII column densities in $M_{\rm vir} \sim 10^{12}$ and $\sim 10^{13}\,M_\odot$ halos based on a set of FIRE-2 and FIRE-3 simulations, run with different physics models, and compared these predictions to observations from the CASBaH (Burchett et al. 2019) and CUBS (Qu et al. 2024) surveys. Our main conclusions are as follows:

1. In $M_{\rm vir} \sim 10^{12}\,M_\odot$ FIRE halos at $z = 0.5$–1.0, Ne VIII traces the relatively smooth, volume-filling phase of the CGM (Figures 1 and 3). At $M_{\rm vir} \sim 10^{13}\,M_\odot$, where the volume-filling phase is typically hotter than optimal for Ne VIII, this ion has a clumpier distribution (Figures 2 and 3).
2. Both in $\sim 10^{12}\,M_\odot$ and $\sim 10^{13}\,M_\odot$ halos in FIRE, Ne VIII is mostly collisionally ionized. Around and beyond $R_{\rm vir}$, some Ne VIII is in PIE. (Figure 4).
3. In FIRE-2, $M_{\rm vir} \sim 10^{12}\,M_\odot$ halos without BH feedback produce higher Ne VIII column densities than in FIRE-3 (Figures 7 and 8). This is largely driven by the higher hot CGM metallicity in FIRE-2 (Figure 5).
4. When comparing CGM observations to predictions from simulations and idealized models, it is important to account for the large uncertainties in halo mass estimates based on galaxy stellar masses. The main source of this uncertainty is scatter in the SMHM relation at stellar masses $\gtrsim 10^{10.5}\,M_\odot$ (Appendix A and Figures 12 and 13).
5. The CUBS and CASBaH surveys report measured O VII column densities, but most of the data are upper limits. Given the large number of upper limits, the FIRE-2 NoBH model for $\sim 10^{12}\,M_\odot$ halos appears broadly consistent with the distribution of measured column densities within an impact parameter of 450 kpc (Figure 9). We note that the median Ne VIII column densities cannot be substantially higher than this model predicts, because this would be in tension with many upper limits. However, since there are some reported detections above the FIRE-2 NoBH 90th percentile column densities, it is possible that the simulations underpredict the scatter in Ne VIII column densities.
6. The FIRE-3 models analyzed in this paper (which use a modified SNe feedback model and/or include AGN feedback) more clearly underpredict these high column densities. Some other cosmological simulations from the literature, e.g., RAMSES (Ford et al. 2013; Liang et al. 2016) and EAGLE (Wijers et al. 2020), also underpredict the highest measured Ne VIII column densities to varying degrees, though one simulation from the AGORA comparison project (ART-I) might overpredict Ne VIII column densities (Strawn et al. 2024).
7. Overall, we find a consistent picture from our analysis of FIRE simulations and idealized, analytic power-law CGM models. Namely, the observed Ne VIII column densities can be mostly reproduced by a CGM with a warm-hot gas fraction and a metallicity whose product is roughly $M_{\rm CGM}/(M_{\rm vir}\Omega_{\rm b}/\Omega_{\rm m}) \times (Z/Z_\odot) \sim 0.1$. These are physically plausible values, realized in particular in FIRE-2 halos.

As they become available, a larger set of simulated halos and/or measured absorbers could improve the robustness of these comparisons. We have also not used all the information in the observations: Burchett et al. (2019) and Qu et al. (2024) also measure the velocities of their absorption systems as a whole, and their component velocities. This kinematic and spatial information will contain information on ongoing gas flows, as well as the current warm-hot halo gas content. We intend to study these absorber kinematics in future work.

Acknowledgments

We thank Zhijie Qu and Hsiao-Wen Chen for sharing their CUBS data, and Phil Hopkins for helpful comments. N.A.W. was supported by a CIERA Postdoctoral Fellowship. J.S. was supported by the Israel Science Foundation (grant No. 2584/21). C.-A.F.-G. was supported by the NSF through grants AST-2108230, AST-2307327, and CAREER award AST-1652522; by NASA through grant Nos. 17-ATP17-0067 and 21-ATP21-0036; by STScI through grant Nos. HST-GO-16730.016-A and JWST-AR-03252.001-A; and by CXO through grant No. TM2-23005X. L.B. was supported by the DOE Computer Science Graduate Fellowship through grant No. DE-SC0020347. I.S. was supported by an NSF Graduate Research Fellowship under grant No. DGE-2234667.

Numerical calculations were run on the Northwestern computer cluster Quest, the Caltech computer cluster Wheeler, Frontera allocation FTA-Hopkins/AST20016 supported by the NSF and TACC, XSEDE/ACCESS allocations ACI-1548562, TGAST140023, and TG-AST140064 also supported by the NSF and TACC, and NASA HEC allocations SMD-16-7561, SMD-17-1204, and SMD-16-7592.

The SMDPL simulation and halo finding have been performed at LRZ Munich within the project pr87yi. The CosmoSim database (www.cosmosim.org) providing the file access is a service by the Leibniz-Institute for Astrophysics Potsdam (AIP).

We made use of PYTHON and C code for this analysis. In particular, we used the following PYTHON modules: ASTROPY (Astropy Collaboration et al. 2013, 2018, 2022), H5PY (Collette 2013), MATPLOTLIB (Hunter 2007), NUMPY (Harris et al. 2020), PANDAS (Wes 2010; The pandas development team 2020), and SCIPY (Virtanen et al. 2020), and the IPYTHON command-line interface (Pérez & Granger 2007).

Data Availability

A number of the FIRE-2 simulations analyzed here are publicly available at http://flathub.flatironinstitute.org/fire (Wetzel et al. 2023). Additional data, including initial conditions and derived data products, are available at https://fire.northwestern.edu/data/. A public version of the GIZMO code is available at http://www.tapir.caltech.edu/~phopkins/Site/GIZMO.html. The scripts used to analyze the simulations are available at http://github.com/nastasha-w/ne8abs_paper. Data shown in the plots are available on reasonable request to the authors.

Appendix A
Estimating Halo Masses from Stellar Masses

Here, we explore some effects of different ways of calculating the halo mass from a galaxy stellar mass. The effects are largest at central galaxy stellar masses of $M_\star \gtrsim 10^{10.5}\,M_\odot$. This is because the halo mass increases more strongly with stellar mass above this mass than below it, and because the scatter in halo masses at fixed stellar mass is higher above this mass than below it. Using the median halo mass at a given stellar mass, and not the median stellar mass at a given halo mass, to estimate halo masses is important. Furthermore, when calculating the best-estimate halo masses and the halo mass uncertainty, it is important to account for the fact that there is a range of possible halo masses for a given galaxy stellar mass.

First, we outline the way we calculate halo mass probability distributions throughout this work. To calculate halo masses for the Burchett et al. (2019, CASBaH) halos, we take their reported log stellar masses and uncertainties, and assume the probability distribution for the true log stellar mass is a Gaussian distribution with the best-estimate stellar mass as the mean and the uncertainty as the variance. We then use the distribution of halo masses at a given central galaxy stellar mass in the UniverseMachine catalog to translate these to probability distributions for parent halo masses. The probability for a given halo mass bin is

$$\begin{aligned} &P(M_\mathrm{h} \in [M_{\mathrm{h},j},\, M_{\mathrm{h},j+1}]) \\ &= \sum_i \{P(M_\star \in [M_{\star,i},\, M_{\star,i+1}]) \\ &\qquad \cdot P(M_\mathrm{h} \in [M_{\mathrm{h},j},\, M_{\mathrm{h},j+1}] \mid M_\star \in [M_{\star,i},\, M_{\star,i+1}])\}, \end{aligned} \tag{A1}$$

where $M_{\mathrm{h},j}$ and $M_{\star,i}$ are edges of bins in halo and stellar mass, respectively. For the probabilities $P(M_\mathrm{h}|\,M_\star)$, we simply use a normalized histogram of the UniverseMachine stellar and halo masses. We note that there are further (systematic) uncertainties associated with the measurement of stellar masses, which we do not account for here. As the relation depends on redshift, we use the halo catalog for the redshift closest to the measured galaxy redshift.

We calculate the Qu et al. (2024, CUBS) halo masses in the same way as the Burchett et al. (2019) masses. However, the estimated probability distribution for the true stellar mass of a galaxy is a bit more complicated. Qu et al. (2024) report different lower and upper error ranges for the stellar masses of some galaxies. The errors they report are 2σ. We therefore approximate the true stellar mass probability distribution for a measured galaxy as two half-log-normal distributions (each with a total probability of 0.5), centered at the measured value and with a variance equal to the upper/lower uncertainty. We estimate the 1σ upper/lower uncertainty σ_tot by combining the reported statistical uncertainty and the systematic uncertainty σ_sys of 0.2 dex of the stellar mass measurements. We estimate the 1σ statistical uncertainty as half the reported 2σ statistical uncertainties $\sigma_{2,\mathrm{stat}}$. This means the variance of each half-log-normal distribution is estimated as $\sigma_\mathrm{tot} = \sqrt{(\,\sigma_{2,\mathrm{stat}}^2/4 + \sigma_\mathrm{sys}^2)}$.

In Figure 12, we show the distribution of the UniverseMachine stellar and halo masses for central galaxies at redshifts 0, 0.5, and 1. The colored lines show relations between stellar mass and halo mass. At galaxy stellar masses $M_\star \gtrsim 10^{10.5}\,M_\odot$, the Burchett et al. (2016) relation used by Burchett et al. (2019) differs considerably from the median halo mass at a given stellar mass. The difference is $\lesssim$0.35 dex at $M_\star \approx 10^{11}\,M_\odot$ at these redshifts, but reaches $\gtrsim$0.6 dex at $M_\star \approx 10^{11.5}\,M_\odot$. The scatter in halo mass at fixed stellar mass

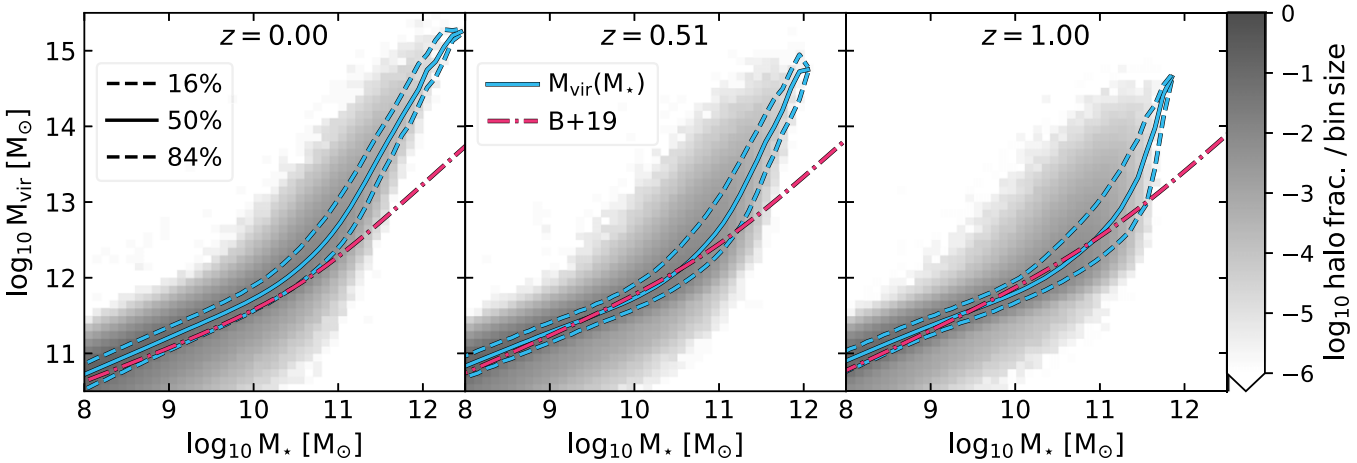

Figure 12. A histogram of the joint (central galaxy) stellar and halo mass distribution (grayscale), taken from the UniverseMachine abundance-matching fits applied to the SMDPL simulations. The cyan lines show different percentiles of $M_\mathrm{vir}(M_\star)$, the halo mass as a function of stellar mass, for the UniverseMachine galaxies. The red curve shows a modified version of the Moster et al. (2013) relation, introduced by Burchett et al. (2016) and used by Burchett et al. (2019) to calculate the virial radii in their Table 1. We convert the Burchett et al. (2019) M_200c halo masses to the Bryan & Norman (1998) definition assuming their mass profiles are NFW (Navarro et al. 1997), with concentrations following Dutton & Macciò (2014). Different relations give different halo masses for a measured stellar mass, and the scatter in halo mass at fixed stellar mass can be large. The differences and scatter are largest at $M_\star \gtrsim 10^{10.5}\,M_\odot$.

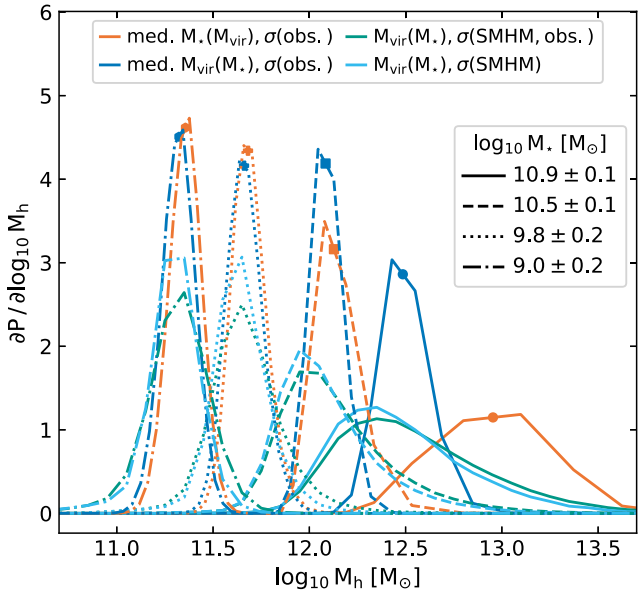

Figure 13. Probability densities for host halo masses of galaxies with different stellar masses (different line styles) from Burchett et al. (2019), assuming a redshift $z = 0.74$. The curves of different colors represent different methods for calculating the halo mass at a given stellar mass. The teal curves account for uncertainty in the measured stellar mass and scatter in the SMHM relation. The cyan curves instead account only for the scatter in the SMHM relation, and the blue curves only account for uncertainty in the measured stellar mass. The orange curves are obtained in the same way as the blue curves, except that we calculate the halo mass at a given stellar mass by mathematically inverting the median stellar mass as a function of halo mass.

is also considerable, especially at $M_\star \gtrsim 10^{10.5}\,M_\odot$: it is $\approx$0.3–0.4 dex at $M_\star \approx 10^{11}\,M_\odot$.

In Figure 13, we calculate the halo mass probability density functions for a few representative galaxy stellar masses and uncertainties from Burchett et al. (2019). Different line styles represent different galaxies, and different colors represent different relations. For the teal curves, we use the method outlined above, which we use throughout this work, except that we assume a single redshift $z = 0.74$ for this example.

For the cyan curve, we ignored errors in the stellar mass measurements. Instead, the probability distribution is just the normalized halo mass histogram at the best-estimate stellar mass. The blue curve effectively does the opposite: we include uncertainties in the true stellar mass, but ignore scatter in the SMHM relation. Here, we still start with a probability for different stellar mass bins. However, we simply convert the stellar mass bin edges to halo mass bin edges using the median halo mass at a given stellar mass. The probabilities remain the same, and we simply divide by the resulting halo mass bin sizes to obtain the probability density. Markers on the blue curves show the halo mass corresponding to the best-estimate stellar mass.

Comparing the blue and cyan curves to the teal, we see that the uncertainty in the halo masses largely comes from the scatter in the SMHM relation at all these masses. However, the SMHM scatter is a more dominant error source at high stellar and halo masses. At masses $M_\star \gtrsim 10^{10.5}\,M_\odot$, obtaining the most likely halo masses also requires accounting for the SMHM scatter, although at lower masses, the median relation suffices for this.

The orange curves show a method of calculating the halo masses which we strongly caution against. The approach is similar to that of the blue curve, using a one-to-one relation between halo mass and stellar mass, and simply propagating the uncertainties in the stellar mass through that relation to obtain the uncertainties in the halo mass. However, here, we use the median stellar mass at a given halo mass to define the relation. We calculate median log stellar masses over a range of log halo masses, and simply linearly interpolate between the resulting points to obtain the halo mass at a given stellar mass.

At low stellar masses ($\lesssim 10^{10.5}\,M_\odot$), this provides reasonable best-estimate halo masses. The lack of inclusion of SMHM scatter does lead to an underestimate of the halo mass uncertainty, but the distributions are very similar to those obtained using the more appropriate one-to-one relation, median halo mass at a given stellar mass. However, at higher stellar masses ($\gtrsim 10^{10.5}\,M_\odot$), the median stellar mass at a given halo mass yields considerably higher halo mass estimates than the median halo mass at a given stellar mass. At these masses, it is important to both use the correct relation, and to account for SMHM scatter.

Burchett et al. (2019) calculated halo masses for their galaxies as well. They use the method of Burchett et al. (2016), who used the SMHM relation of Moster et al. (2013) as a starting point for their relation. Moster et al. (2013) fit a function for the mean stellar mass at a given halo mass, not the mean or median halo mass at a given stellar mass. Burchett et al. (2016) argued that at high galaxy masses, a flatter slope than Moster et al. (2013) found was more appropriate for their isolated galaxies.

We argue that the differences between the Burchett et al. (2016) SMHM relation and the median UniverseMachine halo mass at a given stellar mass (Figure 12) are most likely explained by the difference between the median halo mass at a given stellar mass, and a mathematically inverted median stellar mass as a function of halo mass. We note that the flatter Burchett et al. (2016) slope at high stellar masses reasonably matches the median halo mass at a given stellar mass up to almost $M_\star \approx 10^{11}\,M_\odot$, which is above the $M_\star \approx 10^{10.5}\,M_\odot$ where the $M_\star(M_{\rm vir})$ and $M_{\rm vir}(M_\star)$ median relations diverge.

Appendix B
m12 FIRE-3 NoBH Halos with Higher Halo Masses

In the main body of the paper, we analyzed samples of m12 halos with similar halo masses for the four different physics models we explored. However, these halo masses correspond to different central galaxy stellar masses in the different FIRE models. In particular, the FIRE-2 NoBH model produces higher central galaxy stellar masses in its m12 halos than the FIRE-3 models.

After the simulations in the main body of this paper were run, additional m12 galaxies were simulated with the FIRE-3 NoBH model. Some of these have higher halo masses than our main m12 FIRE-3 NoBH sample, and central galaxy stellar masses comparable to those of our FIRE-2 NoBH halo sample. Three of the halos have resolutions matching those of our other m12 FIRE-3 NoBH halos, the other nine were run at lower resolution. These halos are listed in Table 2.

Here, we test to what extent the difference in central galaxy stellar masses explains the column density difference between the FIRE-2 NoBH and FIRE-3 NoBH m12 halos. In Figure 14, we compare the simulation predictions to good and plausible halo-mass-matched data points in the same way as in Section 4, but we base the halo mass selection range on the range of halo masses in the combined m12 FIRE-3 NoBH sample.

Table 2
As Table 1, but for an Additional Set of m12 FIRE-3 NoBH Halos, Some of Which Have Higher Halo and Stellar Masses than the FIRE-3 NoBH Sample We Analyze in the Main Body of This Work

ICs	Model	Resolution ($M_\odot$)	$z = 1.0$			$z = 0.5$		
			$M_{\rm vir}$ ($M_\odot$)	$M_\star$ ($M_\odot$)	$R_{\rm vir}$ (pkpc)	$M_{\rm vir}$ ($M_\odot$)	$M_\star$ ($M_\odot$)	$R_{\rm vir}$ (pkpc)
m12a	FIRE-3 NoBH	6e4	8.3e11	1.1e10	146	1.2e12	2.3e10	211
m12d	FIRE-3 NoBH	6e4	5.2e11	5.1e9	124	7.0e11	9.7e9	175
m12e	FIRE-3 NoBH	6e4	1.0e12	2.8e9	157	1.4e12	5.6e9	221
m12g	FIRE-3 NoBH	6e4	1.7e12	1.7e10	186	1.9e12	4.5e10	245
m12j	FIRE-3 NoBH	6e4	2.8e11	1.7e9	102	7.1e11	4.8e9	176
m12j	FIRE-3 NoBH	7e3	3.1e11	1.9e9	105	7.1e11	9.1e9	176
m12k	FIRE-3 NoBH	6e4	1.2e12	1.2e10	166	1.9e12	2.5e10	245
m12n	FIRE-3 NoBH	6e4	7.8e11	2.1e9	143	8.9e11	5.8e9	190
m12n	FIRE-3 NoBH	7e3	8.3e11	1.3e10	146	9.3e11	1.5e10	193
m12u	FIRE-3 NoBH	3e4	5.5e11	1.7e9	127	5.2e11	4.3e9	158
m12x	FIRE-3 NoBH	3e4	2.7e11	1.6e9	100	5.0e11	2.4e9	157
m12x	FIRE-3 NoBH	4e3	2.6e11	1.1e9	98	4.1e11	1.4e9	147

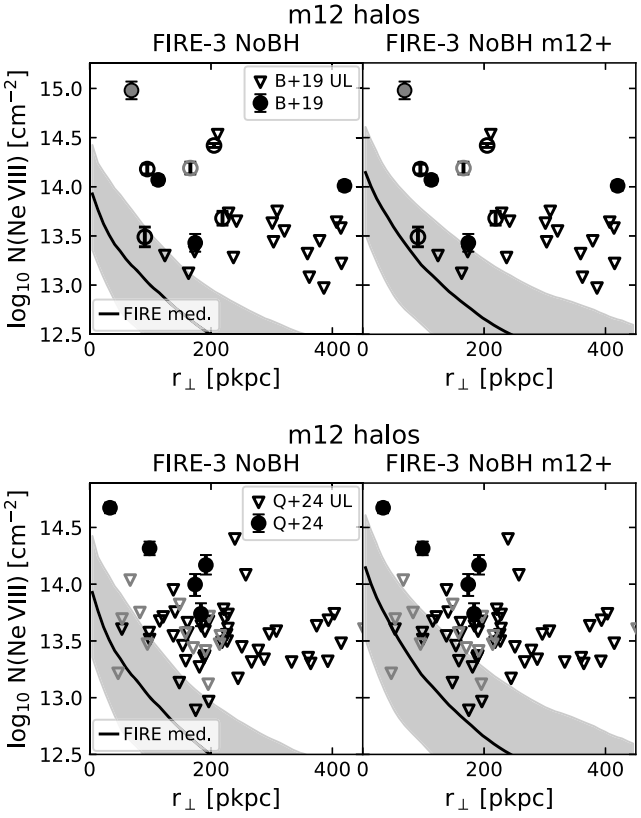

Figure 14. A comparison of the m12 FIRE-3 NoBH halos to the Burchett et al. (2019, B+19; CASBaH) data (top panels) and the Qu et al. (2024, Q+24; CUBS) data (bottom panels). Like Figures 7 and 8, the solid lines show the median for the FIRE models across m12 halos and redshifts 0.5, 0.6, 0.7, 0.8, 0.9, and 1.0. Here, we compare the FIRE-3 NoBH sample from the main body of the paper to the FIRE-3 NoBH m12+ sample listed in Table 2. Including m12 halos with higher halo and stellar masses in the FIRE-3 NoBH sample decreases the difference with the original FIRE-2 NoBH sample, but the FIRE-3 NoBH model still predicts lower Ne VIII column densities than the FIRE-2 NoBH model.

We find that the lower stellar masses in the FIRE-3 NoBH m12 halos might play a part in their lower column densities relative to the FIRE-2 NoBH halos. However, as the stellar yield differences would suggest, the stellar masses do not fully explain the differences (Figure 14).

Appendix C
The Power-law CGM Model

For our simple power-law CGM model, we assume a spherically symmetrical gas distribution within a dark-matter-dominated potential well. We assume power-law circular velocity ($v_{\rm c}$) and entropy (K) profiles:

$$v_{\rm c} \propto r^m, \tag{C1}$$

$$K \propto r^l, \tag{C2}$$

where r is the distance to the halo center, and m and l are the exponents of the circular velocity and entropy profiles, respectively. The entropy is defined as $K = kTn^{-2/3}$, where k is the Boltzmann constant, and n is the gas particle number density.

Our model is based on the analytical cooling flow model of Stern et al. (2019), but generalized to arbitrary entropy profile slopes. We assume a steady-state inflow within the halo. If the only relevant forces are gravity and gas pressure, Newton's second law applied to a gas element gives

$$\rho V \frac{d^2r}{dt^2} = -V\frac{dP}{dr} - \rho V \frac{GM(<r)}{r^2}, \tag{C3}$$

where ρ is density, V is volume, t is time, P is pressure, G is Newton's constant, and $M(<r)$ is the enclosed mass within radius r. Using $v_{\rm c} = \sqrt{GM(<r)/r}$ and the fact that velocity depends only on radius (and not explicitly on time) in this model, we obtain

$$\frac{1}{2}\frac{dv^2}{dr} = -\frac{1}{\rho}\frac{dP}{dr} - \frac{v_{\rm c}^2}{r}. \tag{C4}$$

We multiply both sides of this equation by $r\,/\,c_{\rm s}^2$, where $c_{\rm s} = \sqrt{\gamma P/\rho}$ is the adiabatic sound speed and γ is the adiabatic index. This gives

$$\mathcal{M}^2\frac{d\ln v}{d\ln r} = -\frac{1}{\gamma}\frac{d\ln P}{d\ln r} - \frac{v_{\rm c}^2}{c_{\rm s}^2}, \tag{C5}$$

where $\mathcal{M} = v/c_{\rm s}$ is the Mach number. From here, we make another assumption: that the inflows are subsonic, i.e., $\mathcal{M} \ll 1$. Setting the left-hand term of Equation (C5) to zero, we then

obtain

$$-\frac{1}{\gamma}\frac{d\ln P}{d\ln r} = \frac{v_c^2}{c_s^2}. \quad \text{(C6)}$$

We further assume that the CGM gas is a monatomic ideal gas, meaning $\gamma = \frac{5}{3}$.

Since we are assuming the thermodynamical quantities follow power laws, $d\ln P / d\ln r$ is a constant, meaning v_c^2/c_s^2 must be as well. Since $c_s^2 = \gamma kT/\mu m_H$, where T is the temperature and μ is the mean molecular mass in units of the hydrogen atom mass m_H,

$$T \propto c_s^2 \propto v_c^2 \propto r^{2m}. \quad \text{(C7)}$$

We have assumed here that the mean molecular mass μ is constant. This is reasonable for the warm-hot CGM, where hydrogen and helium are fully ionized, and electron contributions from metals are small.

We can then also solve for the density slope using the entropy, and again assuming $\rho/n = \mu m_H$ is constant. Since $K = kTn^{-2/3}$, we get

$$1 = \frac{d\ln K}{d\ln r} = \frac{d\ln T}{d\ln r} - \frac{2}{3}\frac{d\ln \rho}{d\ln r} = 2m - \frac{2}{3}\frac{d\ln \rho}{d\ln r}, \quad \text{(C8)}$$

which means

$$\rho \propto r^{-3l/2+3m}. \quad \text{(C9)}$$

Finally, this also gives the pressure slope, which is simply the sum of the temperature and density slopes. We use this to solve Equation (C6) for the sound speed:

$$\frac{v_c^2}{c_s^2} = -3m + \frac{9}{10}l. \quad \text{(C10)}$$

This gives the normalization of the temperature profile. Using

$$T_{vir} = \frac{\mu m_H v_c(R_{vir})}{2k}, \quad \text{(C11)}$$

where T_{vir} is the virial temperature and R_{vir} is the virial radius, we get

$$T(R_{vir}) = \frac{6}{5}\frac{1}{\frac{9}{10}l - 3m}T_{vir}. \quad \text{(C12)}$$

If we choose the entropy slope to be $l = 1 + 4m/3$, we recover the power-law cooling flow solution of Stern et al. (2019).

We set the normalization of the density profile using the parameter $f_{CGM} = M_{CGM}/(\Omega_b M_{vir}/\Omega_m)$, where M_{CGM} is the mass of the CGM gas 0.1–1 R_{vir} from the halo center. (Specifically, it is the mass of warm-hot phase we are modeling here.) Ω_b and Ω_m are the cosmic mean baryon and matter densities, respectively, normalized by the critical density. We convert the mass M_{CGM} to a hydrogen number density normalization assuming a hydrogen mass fraction of 0.752.

ORCID iDs

Nastasha A. Wijers https://orcid.org/0000-0001-6374-7185
Claude-André Faucher-Giguère https://orcid.org/0000-0002-4900-6628
Jonathan Stern https://orcid.org/0000-0002-7541-9565
Lindsey Byrne https://orcid.org/0000-0002-8408-1834
Imran Sultan https://orcid.org/0000-0003-2341-1534

References

Asplund, M., Grevesse, N., Sauval, A. J., & Scott, P. 2009, ARA&A, 47, 481
Astropy Collaboration, Price-Whelan, A. M., Lim, P. L., et al. 2022, ApJ, 935, 167
Astropy Collaboration, Price-Whelan, A. M., SipHocz, B. M., et al. 2018, AJ, 156, 123
Astropy Collaboration, Robitaille, T. P., Tollerud, E. J., et al. 2013, A&A, 558, A33
Babyk, I. V., McNamara, B. R., Nulsen, P. E. J., et al. 2018, ApJ, 862, 39
Barret, D., Lam Trong, T., den Herder, J.-W., et al. 2018, Proc. SPIE, 10699, 106991G
Behroozi, P., Wechsler, R. H., Hearin, A. P., & Conroy, C. 2019, MNRAS, 488, 3143
Behroozi, P. S., Wechsler, R. H., & Wu, H.-Y. 2013a, ApJ, 762, 109
Behroozi, P. S., Wechsler, R. H., Wu, H.-Y., et al. 2013b, ApJ, 763, 18
Branchini, E., Ursino, E., Corsi, A., et al. 2009, ApJ, 697, 328
Bregman, J. N., Anderson, M. E., Miller, M. J., et al. 2018, ApJ, 862, 3
Bregman, J. N., Hodges-Kluck, E., Qu, Z., et al. 2022, ApJ, 928, 14
Bregman, J. N., & Lloyd-Davies, E. J. 2007, ApJ, 669, 990
Bryan, G. L., & Norman, M. L. 1998, ApJ, 495, 80
Burchett, J. N., Tripp, T. M., Bordoloi, R., et al. 2016, ApJ, 832, 124
Burchett, J. N., Tripp, T. M., Prochaska, J. X., et al. 2019, ApJ, 877, L20
Byrne, L., Faucher-Giguère, C.-A., Wellons, S., et al. 2023, arXiv:2310.16086
Cen, R., & Fang, T. 2006, ApJ, 650, 573
Chan, T. K., Kereš, D., Hopkins, P. F., et al. 2019, MNRAS, 488, 3716
Chen, H.-W., Zahedy, F. S., Boettcher, E., et al. 2020, MNRAS, 497, 498
Chen, X., Weinberg, D. H., Katz, N., & Davé, R. 2003, ApJ, 594, 42
Colbrook, M. J., Ma, X., Hopkins, P. F., & Squire, J. 2017, MNRAS, 467, 2421
Collette, A. 2013, Python and HDF5 (Sebastopol, CA: O'Reilly)
Crain, R. A., Schaye, J., Bower, R. G., et al. 2015, MNRAS, 450, 1937
Cui, W., Chen, L. B., Gao, B., et al. 2020, JLTP, 199, 502
Das, S., Mathur, S., Gupta, A., Nicastro, F., & Krongold, Y. 2019, ApJ, 887, 257
Davies, J. J., Crain, R. A., Oppenheimer, B. D., & Schaye, J. 2020, MNRAS, 491, 4462
Donahue, M., Horner, D. J., Cavagnolo, K. W., & Voit, G. M. 2006, ApJ, 643, 730
Donahue, M., & Voit, G. M. 2022, PhR, 973, 1
Dutton, A. A., & Macciò, A. V. 2014, MNRAS, 441, 3359
Faerman, Y., Pandya, V., Somerville, R. S., & Sternberg, A. 2022, ApJ, 928, 37
Faucher-Giguère, C.-A. 2020, MNRAS, 493, 1614
Faucher-Giguère, C.-A., Lidz, A., Zaldarriaga, M., & Hernquist, L. 2009, ApJ, 703, 1416
Faucher-Giguère, C.-A., & Oh, S. P. 2023, ARA&A, 61, 131
Ford, A. B., Oppenheimer, B. D., Davé, R., et al. 2013, MNRAS, 432, 89
Gupta, A., Mathur, S., Galeazzi, M., & Krongold, Y. 2014, Ap&SS, 352, 775
Gupta, A., Mathur, S., Krongold, Y., Nicastro, F., & Galeazzi, M. 2012, ApJL, 756, L8
Gupta, A., Mathur, S., & Krongold, Y. 2017, ApJ, 836, 243
Hafen, Z., Faucher-Giguère, C.-A., Anglés-Alcázar, D., et al. 2020, MNRAS, 494, 3581
Harris, C. R., Millman, K. J., van der Walt, S. J., et al. 2020, Natur, 585, 357
Hellsten, U., Gnedin, N. Y., & Miralda-Escudé, J. 1998, ApJ, 509, 56
Hopkins, P. F. 2015, MNRAS, 450, 53
Hopkins, P. F. 2016, MNRAS, 462, 576
Hopkins, P. F. 2024, arXiv:2404.16987
Hopkins, P. F., Butsky, I. S., Panopoulou, G. V., et al. 2022a, MNRAS, 516, 3470
Hopkins, P. F., Chan, T. K., Garrison-Kimmel, S., et al. 2020, MNRAS, 492, 3465
Hopkins, P. F., Quataert, E., & Murray, N. 2012, MNRAS, 421, 3488
Hopkins, P. F., & Raives, M. J. 2016, MNRAS, 455, 51
Hopkins, P. F., Squire, J., Butsky, I. S., & Ji, S. 2022b, MNRAS, 517, 5413
Hopkins, P. F., Torrey, P., Faucher-Giguère, C.-A., Quataert, E., & Murray, N. 2016, MNRAS, 458, 816
Hopkins, P. F., Wetzel, A., Kereš, D., et al. 2018a, MNRAS, 480, 800
Hopkins, P. F., Wetzel, A., Kereš, D., et al. 2018b, MNRAS, 477, 1578
Hopkins, P. F., Wetzel, A., Wheeler, C., et al. 2023, MNRAS, 519, 3154
Hunter, J. D. 2007, CSE, 9, 90
Iwamoto, K., Brachwitz, F., Nomoto, K., et al. 1999, ApJS, 125, 439
Ji, S., Chan, T. K., Hummels, C. B., et al. 2020, MNRAS, 496, 4221
Klypin, A., Yepes, G., Gottlöber, S., Prada, F., & Heß, S. 2016, MNRAS, 457, 4340
Kraft, R., Markevitch, M., Kilbourne, C., et al. 2022, arXiv:2211.09827

Kroupa, P. 2001, MNRAS, 322, 231
Leitherer, C., Schaerer, D., Goldader, J. D., et al. 1999, ApJS, 123, 3
Leung, S.-C., & Nomoto, K. 2018, ApJ, 861, 143
Liang, C. J., Kravtsov, A. V., & Agertz, O. 2016, MNRAS, 458, 1164
Martizzi, D., Faucher-Giguère, C.-A., & Quataert, E. 2015, MNRAS, 450, 504
McAlpine, S., Helly, J. C., Schaller, M., et al. 2016, A&C, 15, 72
McKinney, W. 2010, in Proc. 9th Python in Science ConferenceSciPy 2010, ed. W. Stéfan van der & M. Jarrod (Austin, TX: SciPy), 56
McQuinn, M. 2014, ApJL, 780, L33
Miller, M. J., & Bregman, J. N. 2015, ApJ, 800, 14
Mitchell, P. D., & Schaye, J. 2022, MNRAS, 511, 2948
Moster, B. P., Naab, T., & White, S. D. M. 2013, MNRAS, 428, 3121
Mroczkowski, T., Nagai, D., Basu, K., et al. 2019, SSRv, 215, 17
Muratov, A. L., Kereš, D., Faucher-Giguère, C.-A., et al. 2015, MNRAS, 454, 2691
Muratov, A. L., Kereš, D., Faucher-Giguère, C.-A., et al. 2017, MNRAS, 468, 4170
Nandra, K., Barret, D., Barcons, X., et al. 2013, arXiv:1306.2307
Navarro, J. F., Frenk, C. S., & White, S. D. M. 1997, ApJ, 490, 493
Nelson, D., Byrohl, C., Ogorzalek, A., et al. 2023, MNRAS, 522, 3665
Nicastro, F., Krongold, Y., Mathur, S., & Elvis, M. 2017, AN, 338, 281
Nomoto, K., Tominaga, N., Umeda, H., Kobayashi, C., & Maeda, K. 2006, NuPhA, 777, 424
Pandya, V., Somerville, R. S., Anglés-Alcázar, D., et al. 2020, ApJ, 905, 4
Pérez, F., & Granger, B. E. 2007, CSE, 9, 21
Perna, R., & Loeb, A. 1998, ApJL, 503, L135
Ploeckinger, S., & Schaye, J. 2020a, Rates and fractions, V1, Harvard Dataverse, doi:10.7910/DVN/GR3L5N
Ploeckinger, S., & Schaye, J. 2020b, MNRAS, 497, 4857
Power, C., Navarro, J. F., Jenkins, A., et al. 2003, MNRAS, 338, 14
Prochaska, J. X., Burchett, J. N., Tripp, T. M., et al. 2019, ApJS, 243, 24
Qu, Z., & Bregman, J. N. 2018, ApJ, 856, 5
Qu, Z., Chen, H.-W., Johnson, S. D., et al. 2024, ApJ, 968, 8
Ravi, V. 2019, ApJ, 872, 88
Rodríguez-Puebla, A., Behroozi, P., Primack, J., et al. 2016, MNRAS, 462, 893
Schaye, J., Crain, R. A., Bower, R. G., et al. 2015, MNRAS, 446, 521
Smith, R. K., Abraham, M. H., Allured, R., et al. 2016, Proc. SPIE, 9905, 99054M
Stern, J., Faucher-Giguère, C.-A., Hennawi, J. F., et al. 2018, ApJ, 865, 91
Stern, J., Fielding, D., Faucher-Giguère, C.-A., & Quataert, E. 2019, MNRAS, 488, 2549
Strawn, C., Roca-Fàbrega, S., Primack, J. R., et al. 2024, ApJ, 962, 29
Su, K.-Y., Hopkins, P. F., Bryan, G. L., et al. 2021, MNRAS, 507, 175
Su, K.-Y., Hopkins, P. F., Hayward, C. C., et al. 2019, MNRAS, 487, 4393
Sukhbold, T., Ertl, T., Woosley, S. E., Brown, J. M., & Janka, H. T. 2016, ApJ, 821, 38
The EAGLE team. 2017, arXiv:1706.09899
The Lynx Team 2018, arXiv:1809.09642
The pandas development team 2020, pandas-dev/pandas: Pandas, latest, Zenodo, doi: 10.5281/zenodo.3509134
Torrey, P., Hopkins, P. F., Faucher-Giguère, C.-A., et al. 2020, MNRAS, 497, 5292
Tripp, T. M., Meiring, J. D., Prochaska, J. X., et al. 2011, Sci, 334, 952
Tsai, J. C., & Mathews, W. G. 1995, ApJ, 448, 84
Tumlinson, J., Peeples, M. S., & Werk, J. K. 2017, ARA&A, 55, 389
Upton Sanderbeck, P. R., McQuinn, M., D'Aloisio, A., & Werk, J. K. 2018, ApJ, 869, 159
van de Voort, F., Bieri, R., Pakmor, R., et al. 2021, MNRAS, 501, 4888
Verner, D. A., Tytler, D., & Barthel, P. D. 1994, ApJ, 430, 186
Virtanen, P., Gommers, R., Oliphant, T. E., et al. 2020, NatMe, 17, 261
Voit, G. M. 2019, ApJ, 880, 139
Wellons, S., Faucher-Giguère, C.-A., Hopkins, P. F., et al. 2023, MNRAS, 520, 5394
Wendland, H. 1995, AdCMa, 4, 389
Werk, J. K., Prochaska, J. X., Tumlinson, J., et al. 2014, ApJ, 792, 8
Wetzel, A., Hayward, C. C., Sanderson, R. E., et al. 2023, ApJS, 265, 44
Wiersma, R. P. C., Schaye, J., & Smith, B. D. 2009, MNRAS, 393, 99
Wijers, N. A., & Schaye, J. 2022, MNRAS, 514, 5214
Wijers, N. A., Schaye, J., & Oppenheimer, B. D. 2020, MNRAS, 498, 574
Yao, Y., & Wang, Q. D. 2005, ApJ, 624, 751
Zhang, Y., Comparat, J., Ponti, G., et al. 2024, arXiv:2401.17308
Zhu, B., & Springel, V. 2024, arXiv:2404.13837
Zhu, Z., Xu, H., Hu, D., et al. 2021, ApJ, 908, 17